AGU PUBLICATIONS

JGR

Journal of Geophysical Research: Oceans

RESEARCH ARTICLE

10.1002/2015JC010992

Key Points:

- GOCI images are used to retrieve critical shear stress for erosion with observation and modeling
- The retrieved result is validated with soil mechanics of field survey data
- GOCI-retrieved results provides better simulation than uniform critical shear stress

Correspondence to:
J. Ge,
jzge@sklec.ecnu.edu.cn

Citation:
Ge, J., F. Shen, W. Guo, C. Chen, and P. Ding (2015), Estimation of critical shear stress for erosion in the Changjiang Estuary: A synergy research of observation, GOCI sensing and modeling, *J. Geophys. Res. Oceans*, *120*, 8439–8465, doi:10.1002/2015JC010992.

Received 21 MAY 2015
Accepted 2 DEC 2015
Accepted article online 9 DEC 2015
Published online 29 DEC 2015

Estimation of critical shear stress for erosion in the Changjiang Estuary: A synergy research of observation, GOCI sensing and modeling

Jianzhong Ge[1], Fang Shen[1], Wenyun Guo[1], Changsheng Chen[1,2,3], and Pingxing Ding[1]

[1]State Key Laboratory of Estuarine and Coastal Research, East China Normal University, Shanghai, China, [2]School for Marine Science and Technology, University of Massachusetts-Dartmouth, New Bedford, Massachusetts, USA, [3]International Center for Marine Studies, Shanghai Ocean University, Shanghai, People's Republic of China

Abstract Simulating the sediment transport in a high-turbidity region with spatially varying bed properties is challenging. A comprehensive strategy that integrates multiple methods is applied here to retrieve the critical shear stress for erosion, which plays a major role in suspended sediment dynamics in the Changjiang Estuary (CE). Time-series of sea surface suspended sediment concentration (SSC) were retrieved from the Geostationary Ocean Color Imager (GOCI) satellite data at hourly intervals (for 8 *h* each day) and combined with hydrodynamic modeling of high-resolution CE Finite-Volume Community Ocean Model (CE-FVCOM) to estimate the near-bed critical shear stress in the clay-dominated bed region (plasticity index $>7\%$). An experimental algorithm to determine the in situ critical shear stress via the plasticity index method was also used to verify the GOCI-derived critical shear stress. Implemented with this new critical shear stress, the sediment transport model significantly improved the simulation of the distribution and spatial variability of the SSC during the spring and neap tidal cycles in the CE. The results suggest that a significant lateral water exchange between channels and shoals occurred during the spring flood tide, which led to a broader high-SSC area in the CE throughout the water column.

1. Introduction

Many coastal and estuarine regions, such as the Changjiang Estuary (CE) [*Chen et al.*, 1999], the Yellow River Estuary [*Pang et al.*, 2001; *Wang and Wang*, 2010] and the Dutch coastal zone [*Van Kessel et al.*, 2011] are highly sedimentary, in which the sediment concentration and transport vary significantly in space and with time. The dynamics controlling the spatial distribution and temporal variation of the sediment concentration are quite complex, involving not only fully nonlinear current-wave interactions but also depending on water and bed properties and anthropogenic impacts. In addition to the hydrodynamic environmental processes, the sediment erosion and deposition at the seabed play a critical role in controlling sedimentation, particularly in a turbidity-characterized estuary.

The Changjiang River mouth is a typical high-turbidity water estuary that receives sediment up to an annual amount of ~200 million tons from its upstream region [*Chen et al.*, 1999]. The sediment in this estuary is highly suspended, occurring mainly around the river mouth and over the inner shelf region [*Chen et al.*, 1999]. The physics controlling the SSC variation have been extensively examined in both field measurements and process-oriented mechanism studies [e.g., *Shen et al.*, 1993; *Kong et al.*, 2006; *Chen et al.*, 2006a; *Yang et al.*, 2007; *Liu et al.*, 2011; *Song and Wang*, 2013]. The SSC in the CE is a key factor that directly influences navigation, coastline evolution [*Liu et al.*, 2011], and the local ecosystem, particularly for frequently occurring harmful algal blooms [*Chen et al.*, 2003]

It is a challenge to simulate the spatial distribution and temporal variation of the SSC in high-turbidity estuaries. Many fully hydrodynamics-sediment coupled models have been developed to simulate the sediment transport [*Amoudry and Souza*, 2011], including, for example, COHERENS [*Luyten et al.*, 1999], Delft3D [*Deltares*, 2012], ECOMSed/ECOM-si [*HydroQual*, 2002; *Zheng et al.*, 2003], EFDC [*Hamrick*, 1992a,b], FVCOM [*Chen et al.*, 2003, 2006b, 2013], POM [*Wang*, 2002], and ROMS [*Warner et al.*, 2008]. Delft3D [*Hu et al.*, 2009], ECOMSed [*Du et al.*, 2010] and POM [*Song and Wang*, 2013] were applied to study the sediment transport in the CE. All these studies showed that the simulation results were sensitive to the parameterization in the source term of the seabed-water interface in the sediment transport equation. In a local region where the sediment was distributed uniformly in space, it was found that by tuning the parameter in Partheniades' formula for the erosion rate, the models were capable of reproducing the vertical distribution and temporal variability of the SSC. The Partheniades' formula [*Kandiah*, 1974; *Ariathurai and Arulanandan*, 1978] is given as

$$E=M\left(\frac{\tau_b-\tau_{ce}}{\tau_{ce}}\right) \quad \text{for } \tau_b > \tau_{ce} \tag{1}$$

where E is the erosion rate (kg m^{-2} s^{-1}); M is an empirical parameter for the erosion with the same unit as E; τ_b (N/m^2) is the mean bottom shear stress acting on the bed surface; and τ_{ce} (N/m^2) is the critical (threshold) shear stress for erosion. τ_{ce} and M are the two critical parameters controlling the erosion loading. In the previous model experiments, these two parameters were specified as constant values and the validation was done only by comparing the tuned SSC profile at individual measurement sites. In fact, the values of τ_{ce} and M are both functions of the bed density, porosity, composition, consolidation and evolution of the sediment under the complex and mixed effects of the physical and biological interaction process. Since these properties generally vary in space and with time, ignoring the spatial variation of τ_{ce} and M, these sediment transport models were set up with extensive evaluations against the observed data for the CE [*Song and Wang*, 2013] and other regions [*Lopes et al*., 2006; *Van Kessel et al*., 2011; *Pinto et al*., 2012]. Determining τ_{ce} for different types of sediment is not a trivial task. For example, the value of τ_{ce} for the natural mud and sand reported in the literature varies over a wide range [*Parchure and Mehta*, 1985]. Typically, it has been determined via laboratory experiments or soil mechanics with various specified parameters [*Maa et al*., 1995; *Kim et al*., 2000; *Sarmiento and Falcon*, 2006; *de Linares and Belleudy*, 2007; *Andersen et al*., 2007; *Maa et al*., 2008; *Thoman and Niezgoda*, 2008; *Van Prooijen and Winterwerp*, 2010; *Amos et al*., 2010; *Jacobs et al*., 2011; *Letter and Mehta*, 2011; *Grabowski et al*., 2012; *Winterwerp et al*., 2012; *Salehi and Strom*, 2012; *Soulsby et al*., 2013]. When sufficient measurement data are available and adequate bed property information is known, one could always tune τ_{ce} to resolve the spatially nonuniform SSC [*Lumborg*, 2005; *Chao et al*., 2008; *Hu et al*., 2009; *Du et al*., 2010; *Van der Wal et al*., 2010; *Carniello et al*., 2012; *Ramakrishnan and Rajawat*, 2012]. However, in most cases, these tunings are done empirically to best fit the data with the model. In summary, the difficulty in the determination of τ_{ce} or M limits the applicability of existing models to the large-scale sediment simulation, particularly in the CE where the bed properties vary remarkably in space and with time [*Chen et al*., 1999].

In the recent decade, the satellite-derived ocean color image data, such as those obtained from the Sea-viewing Wide Field-of-view Sensor (SeaWiFS), Moderate Resolution Imaging Spectroradiometer (MODIS) on board the NASA Terra (1999-) and Aqua (2002-) satellites, and MEdium Resolution Imaging Spectrometer (MERIS) on board the European Space Agency (ESA)'s Envisat platform (2002–2012), have been increasingly used to study the distribution of the surface sediment concentration in the coastal and estuarine regions [*Chen et al*., 2004; *Doxaran et al*., 2002, 2009; *Doerffer and Schiller*, 2007, 2008; *Shen et al*., 2010, 2013]. A simple radiative transfer model based algorithm, which was developed and calibrated particularly for the high-turbidity water in the CE, can estimate the sediment concentration based on the spectra band of remote sensing reflectance [*Shen et al*., 2010, 2013]. In 2010, the Korea Ocean Research and Development Institute (KORDI) launched a satellite with the Geostationary Ocean Color Imager (GOCI), which covered the Northeast Asian Seas. The GOCI provides a high spatial and temporal coverage of the sea surface sediment reflectance with a horizontal resolution of ~500 m at hourly intervals for 8 h each day in the East China and Japan Seas [*Cho et al*., 2010; *Ryu et al*., 2012]. Converting the remote-sensing reflectance to the sediment concentration using the spectral interpreting algorithm, the GOCI has been used to monitor the change of the sea surface sediment concentration in the CE [*Choi et al*., 2012; *He et al*., 2013].

We have developed a new methodology to integrate the GOCI data with the hydrodynamic modeling and field measurement data and used it to estimate the critical bottom shear stress for erosion. The goal of this effort is to provide a better spatial- resolving bottom boundary condition for sediment suspension in the high-turbidity water, where the bed property varies significantly in space in the CE sediment model. The threshold of the shear stress for erosion estimated by this new method was compared with the value determined by the soil mechanics theory [*Smerdon and Beasley*, 1959; *Torfs*, 1995; *Jacobs et al*., 2011]. It was then indirectly verified by comparing the model-simulated spatial distribution and temporal variation of the SSC with the field measurement data in the CE and adjacent inner shelf region.

This paper summarizes the key findings we obtained from the sediment simulation of the CE-FVCOM sediment model, with an improved estimation of the critical bottom shear stress for erosion using the new integration method. The structure of the paper is organized as follows. In section 2, the data sets obtained from the GOCI and field surveys, are described. In section 3, the retrieval integrated algorithm used to estimate the bottom shear stress threshold for erosion is presented. In section 4, the results are compared with the values derived from the soil mechanics theory. And the model-simulated SSC is validated with the observations taken at survey sites. The dynamic mechanism controlling the sediment transport in the CE is examined. The performance and shortcomings of this retrieval algorithm are discussed in section 5, and the conclusion is summarized in section 6.

2. The GOCI and Field Survey Data

The data used in this study were from two sources: (1) the satellite-derived GOCI and (2) the shipboard surveys. To test the integrated methodology for the estimation of critical bottom stress for erosion, we selected 5 April 2011 as a test period during which 8 hourly clear sky snapshots of GOCI image data were taken from 8:16 AM to 03:16 PM (Figure 1). The images were derived from 8 visible and near-infrared bands with wavelengths in the range of 412–865 nm in the CE and adjacent shelf region. They were converted to the SSC using the proposed retrieval algorithm of a semiempirical radiative transfer [*Shen et al*., 2010], given as

$$C_{ss}=\frac{(2\alpha/\beta)R_{rs}}{(\alpha-R_{rs})^2}, \tag{2}$$

where C_{ss} (g/L) is the SSC; R_{rs} is the remote-sensing reflectance (s/r); and the two parameters α and β are constants with the same unit as R_{rs} (s/r). The parameters were determined optimally by the least-square fitting via in situ synchronous measurements of R_{rs} and C_{ss} [*Shen et al*., 2010]. This approach was similar to that used in Lake Michigan for the SeaWiFS data by *Chen et al*. [2004]. Considering the saturation case of R_{rs} with shorter wavelengths in extremely turbid water and the insensitivity of R_{rs} with longer wavelengths in relatively clear waters, we combined the waveband switching and multiband weighted integration scheme recommended by *Shen et al*. [2010, 2013].

The GOCI-derived SSC indicated that during the selected period, the SSC in the CE changed significantly with time: increasing in the morning over a period from 08:16 AM to 12:16 PM at noon, decreasing in the early afternoon over a period from 01:16 PM to 02:16 PM, and then increasing again after 03:16 PM (Figure 1). The SSC also varied remarkably in space. The SSC in the CE was in a range of 0.1–1.0 g/L, but the SSC in and around the Hangzhou Bay reached ~1.5 g/L. The SSC in the Hangzhou Bay initially followed an ascending pattern during the first 4 h, but maintained a decline afterward, as the core of the maximum SSC shifted landward.

We have conducted four shipboard surveys to collect the data of the bed properties including the median grain size, density, porosity, and clay content in the CE and its adjacent shelf region. The three surveys were conducted in the summer season during 8–18 July 2011, 12–18 August 2012, and 13–20 July 2014, and the one was carried out in the winter season during 10–20 January 2013. These sampling sites are shown in Figure 2.

The observations show that the sea floor in the CE and adjacent bay/shelf was mainly characterized by a fine-size sediment composition (Figure 3a), with a minimum size of ~15 μm observed in the Hangzhou Bay and near the river mouth close to the outlet of the North Passage. The main CE channels, which include the South Branch, North Channel, and South and North Passages, had similar bed properties with fine sand of grain sizes in the range of ~40–125 μm. The sand generally covered the northeastern region off the estuary with a size of >200 μm. The clay content exhibited a similar pattern to the distribution of the median grain sizes (Figure 3b). High clay content dominated the bed sediment in the Hangzhou Bay, the outer estuarine area of the CE, and the offshore region of Jiangsu's coast. Low clay content covered the bed surface in the South Branch of the CE and the inner shelf of the East China Sea (ECS). The river mouth, including the South Passage, the North Passage and the North Channel, was the low-high clay transition zone where the clay content accounted for 10% ~ 40% of the total sediment. The clay content in the North Passage showed a highly spatial nonuniform pattern, high at the entrance and in the outlet region and low in the middle area.

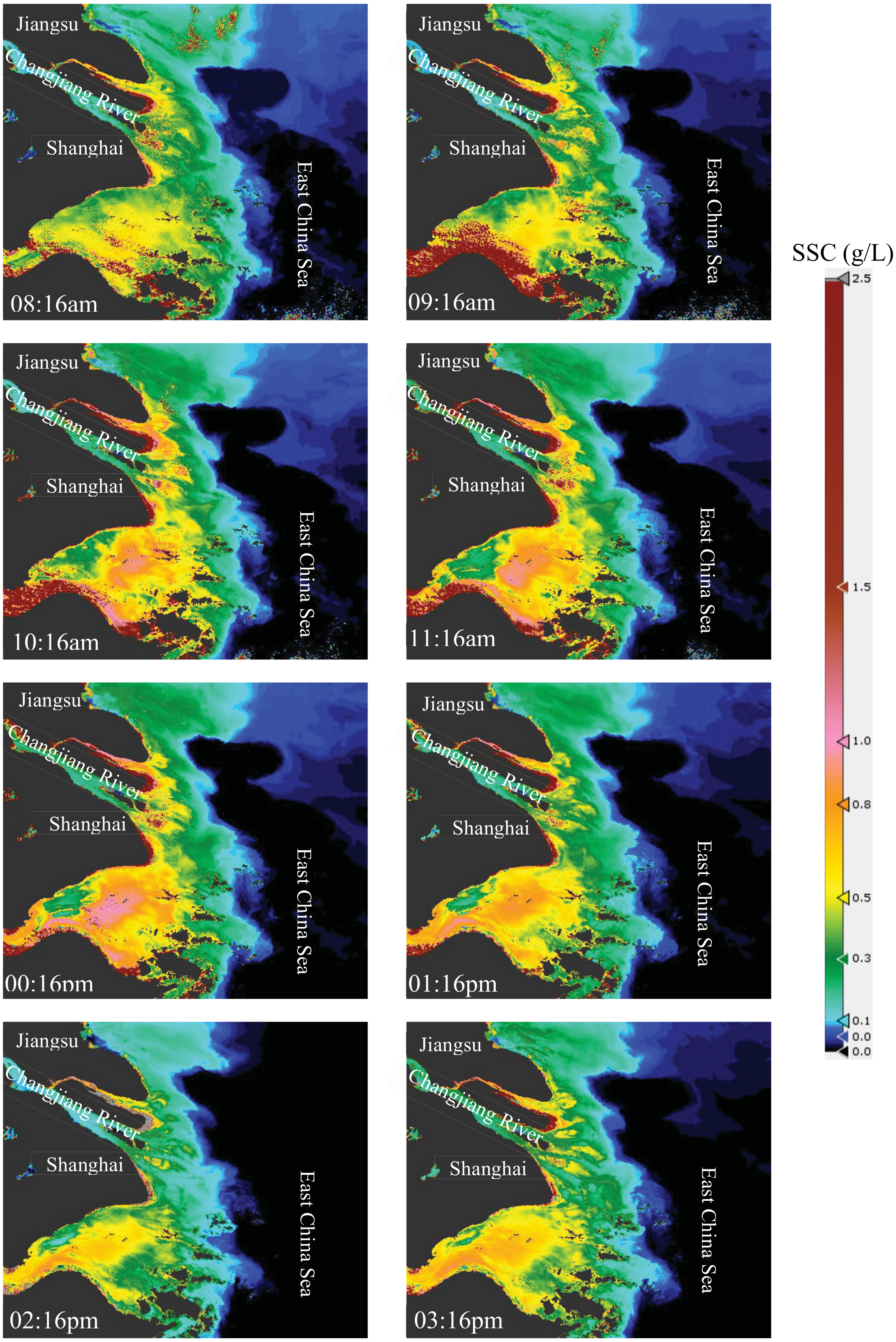

Figure 1. Distributions of suspended sediment concentration (SSC) retrieved from the Geostational Ocean Color Image (GOCI) satellite over the time period of 08:16 AM–03:16 PM on 5 April 2011.

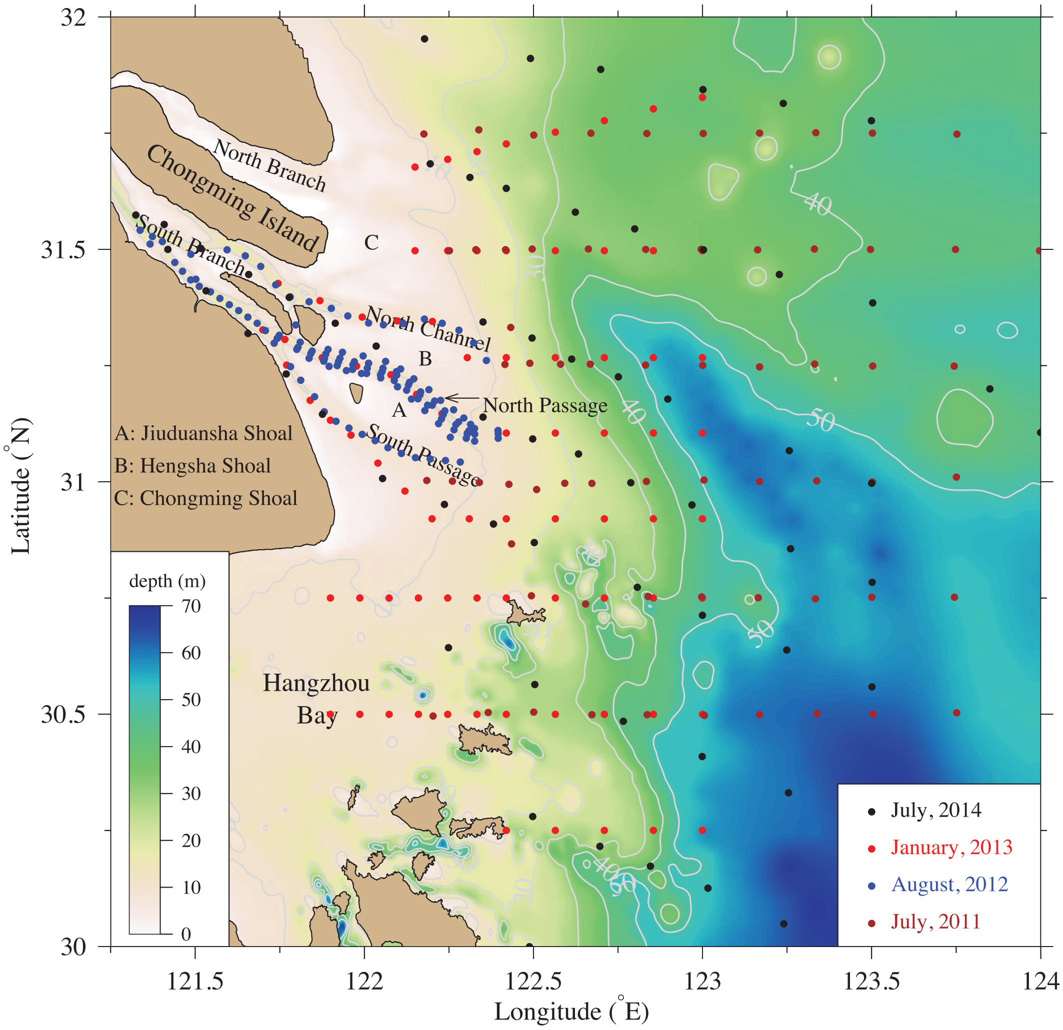

Figure 2. Bathymetry and survey sites in the Changjiang Estuary and Hangzhou Bay. The brown points indicate the measurement sites during 8–18 July 2011. The blue, red and black points are for 12–18 August 2012, 10–20 January 2013, and 13–20 July 2014.

3. An Integrated GOCI-Model Method to Estimate τ_{ce}

According to the governing equation of the three dimensional suspended sediment transport, the sediment content and local change at the given location and time could be determined by the following:

$$\frac{\partial C}{\partial t}+\nabla_H\cdot(\boldsymbol{u}C)+\frac{\partial(\omega-\omega_s)C}{\partial z}=\frac{\partial}{\partial z}\left(K_M\frac{\partial C}{\partial z}\right) \tag{3}$$

where ∇_H represents the horizontal derivative; C (g/L) is the concentration of the suspended sediment; $\boldsymbol{u}$ (m/s) is the horizontal water velocity vector; ω (m/s) and ω_s (m/s) ω are the vertical water and sediment-settling velocities, respectively; and K_M (m^2/s) is the vertical eddy viscosity. The horizontal diffusion term was omitted from this study because it was orders of magnitude smaller than advection, erosion, deposition and settling. Following the derivations described in Appendix A, the depth-integrated advection term (*Adv*) over a time period from $t_1$to t_2 is given as

$$Adv=\int_{t_1}^{t_2}\left(\nabla_H\cdot\int_{-h}^{\zeta}C\boldsymbol{u}dz\right)dt, \tag{4}$$

and the erosion (*Ero*) and deposition (*Dep*) terms over the same period are determined as

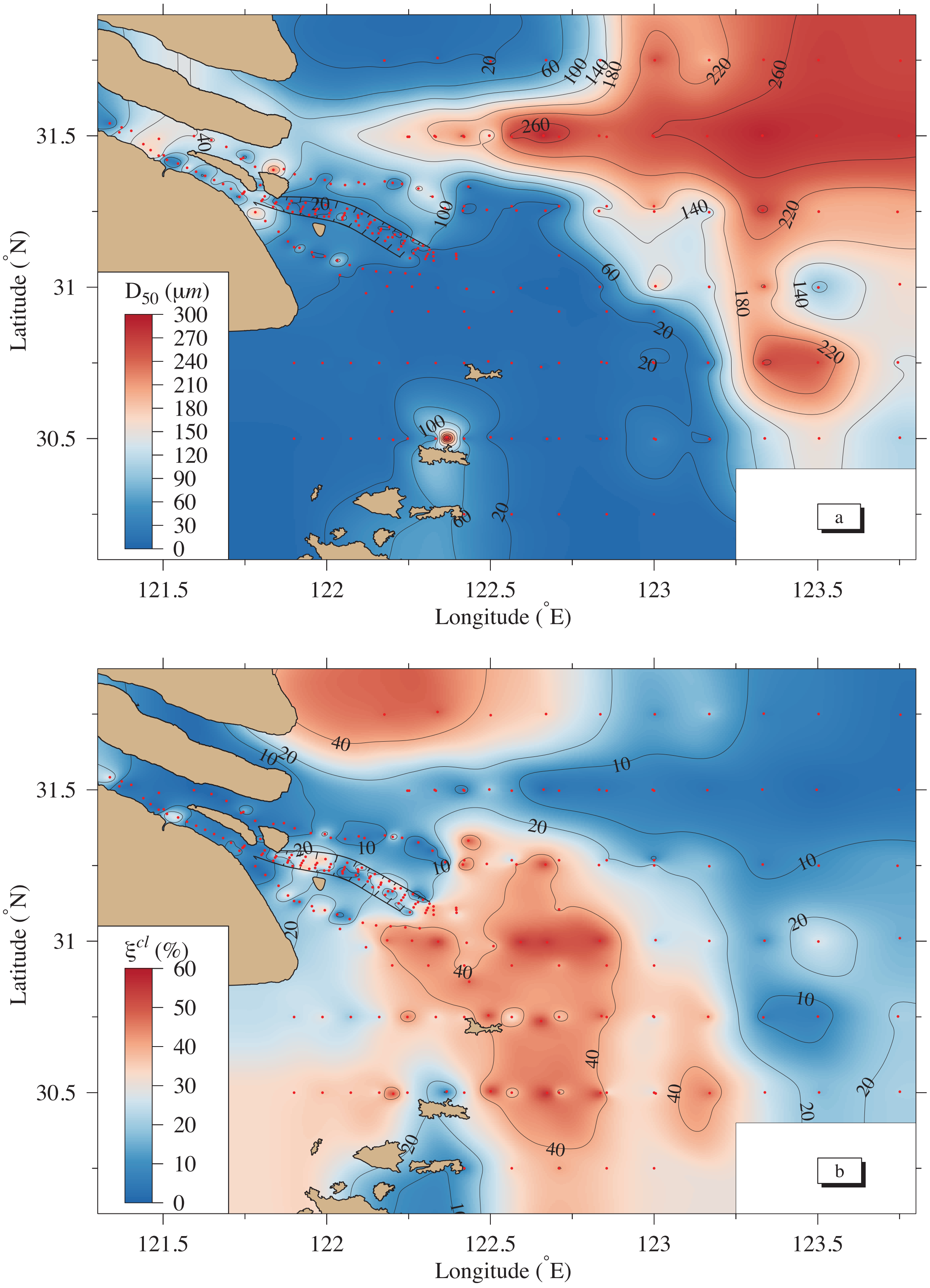

Figure 3. Distributions of media grain size (d_{50}) at the (a) seabed surface and (b) clay content (ξ_{cl}) of the mud samples.

$$Ero = \int_{t_1}^{t_2} E dt = \int_{t_1}^{t_2} M \frac{\tau_b - \tau_{ce}}{\tau_{ce}} dt; \tag{5}$$

$$Dep = \int_{t_1}^{t_2} D dt = \int_{t_1}^{t_2} C_{bs} \omega_{bs} dt, \tag{6}$$

where D and E represent the deposition and erosion rates, respectively; h (m) is the water depth; ζ (m) is the water surface elevation; τ_b (N/m^2) is the bottom shear stress under the realistic wave-current interaction condition; C_{bs}(g/L) is the near-bed suspended sediment concentration; and ω_{bs} (m/s) is the near-bed vertical settling velocity.

The net change of the suspended sediment mass in the water column (hereafter named "ΔS_{sed}") equals to the sum of advection, diffusion and erosion minus deposition at the bed surface. It could also be computed by taking the difference of the vertically integrated SSCs between t_1 and t_2, that is

$$\Delta S_{sed} = \int_{-h}^{\zeta(t_2)} C(t_2) \mathrm{d}z - \int_{-h}^{\zeta(t_1)} C(t_1) dz. \tag{7}$$

In equation (5), given M, τ_b and T, τ_{ce} can be calculated by

$$\tau_{ce} = \frac{M\tau_b}{Ero/(t_2 - t_1) + M}. \tag{8}$$

In an estuary, it is difficult to accurately calculate the erosion rate coefficient (M) since it depends on the consolidation of bed and sediment composition, such as the fluid mud between the bed and water column [*Houwing and Rijn*, 1998]. The typical value of this parameter was in a range of $10^{-6} - 10^{-3}$ kg/(s·m^2). This means that due to a wide range of M, the critical shear stress for erosion in equation (8) could be of 1–3 orders of magnitude difference. In previous studies [e.g., *Lopes et al*., 2006; *Van Kessel et al*., 2011; *Pinto et al*., 2012; *Song and Wang*, 2013], the erosion rate was assumed as a constant, with, for example, a value of 2×10^{-4} kg/(s·m^2) in *Song and Wang* [2013]. In addition, when both Ero and τ_b are positive, then τ_{ce} could always be a positive value. If one could reasonably estimate the erosion mass and bottom shear stress over a specific duration of time, one could use equation (8) to calculate the critical shear stress for erosion.

With math derivations described in Appendix A, the erosion term can be expressed as

$$Ero = \int_{-h}^{\zeta(t_2)} C(t_2) dz - \int_{-h}^{\zeta(t_1)} C(t_1) dz + \int_{t_1}^{t_2} \left(\nabla_H \cdot \int_{-h}^{\zeta} C\mathbf{u} dz \right) dt + \int_{t_1}^{t_2} D dt \tag{9}$$

Substituting equation (9) into equation (8), we have

$$\tau_{ce} = \frac{M\tau_b}{\left(\int_{-h}^{\zeta(t_2)} C(t_2) dz - \int_{-h}^{\zeta(t_1)} C(t_1) dz + \int_{t_1}^{t_2} \left(\nabla_H \cdot \int_{-h}^{\zeta} C u dz \right) dt + \int_{t_1}^{t_2} D dt \right) / (t_2 - t_1) + M}. \tag{10}$$

Here $C(z)$ illustrates the vertical profiles of the suspended sediment concentration. It is an unknown variable, which is determined by either observations or a sediment model. In equation (10), when the difference of the vertically integrated *SSCs* at two time steps is known, we could use an empirical approach to estimate this difference. The Rouse formula [*Rouse*, 1938] was widely used to estimate the SSC profiles in previous studies. This method was robust in approximating the vertical distribution of the SSC in the CE [*Shi et al*., 2003; *Li and Zhang*, 1998]. This formula is given as

$$C(z) = s_a \left(\frac{D - Z'}{Z'} \frac{a}{D - a} \right)^n, \tag{11}$$

where $D = H + \zeta$ is the total water depth; $z'(m)$ is the height above the seabed; $a(m)$ is the reference depth below the sea surface; and S_a (g/L) is the known suspended sediment concentration at the reference depth $z = a$. n is the so-called Rouse number defined as

$$n = w_s / \kappa u_* \tag{12}$$

where κ is the von Karman constant; $u_* = \sqrt{\tau_b / \rho}$ is the friction velocity; τ_b is the bottom stress; and ρ is the water density. n indicates the balance between the turbulent mixing and vertical settling of sediment

Table 1. Linear Regression Between Optical Turbidity (NTU) of OBS and Sediment Concentration Measured From Water Samples

	Spring Tide				Neap Tide			
Station	Count	Slope	Intercept	R^2	Count	Slope	Intercept	R^2
X1203	133	0.0013	−0.0169	0.79	151	0.0015	−0.0208	0.87
X1204	156	0.0013	0.0033	0.86	144	0.0015	−0.0129	0.91
X1205	156	0.0011	0.0206	0.62	149	0.0013	0.0094	0.73
X1206	85	0.0009	0.0969	0.44	156	0.0013	−0.0496	0.94
X1207	156	0.0014	0.0322	0.78	156	0.0016	−0.038	0.87
X1208	150	0.0012	0.1351	0.72	156	0.0008	0.0846	0.72
X1210	156	0.0016	0.0392	0.71	156	0.0016	0.0956	0.92
X1211	156	0.0015	0.1001	0.83	156	0.0015	0.0867	0.85
X1212	162	0.0011	0.1048	0.43	156	0.0015	0.0909	0.55
X1213	150	0.0020	0.0878	0.85	144	0.0015	0.1088	0.72

particles. Equation (11) is only valid under a condition with nonzero a and u_*. In this study, a was set at a height of 0.2 m below the sea surface and S_a was defined as the GOCI-derived SSC. n was calculated by equation (12) with up-bound and low-bound constraints from the observations. During the field measurement surveys, extensive sediment profiles were collected from the upstream river channel to the outer estuary using the optical backscatter sensor (OBS) instrument, which also covered the spring-neap tidal cycles. The OBS was initially calibrated to NTU standards before field deployment. The optically retrieved nephelometric turbidity unit (NTU) from the OBS was calibrated using simultaneously collected water samples. A regression analysis was conducted for optical turbidities and sediment concentration water samples (g/L), and the results indicated a linear relationship between these two variables at a 95% confidence level (Table 1). Using this linear regression, we converted all high-resolution vertical OBS profiles at the measurement sites to the sediment concentrations.

For the known S_a and a, we calculated n by taking the nature logarithm on both sides of equation (11), which yielded

$$n=\frac{\ln\left(\bar{C}\right)}{\ln\left[\hat{a}\left(D-z'\right)/z'\right]} \tag{13}$$

where $\bar{C}$ is the nondimensional value of the SSC scaled by S_a, and $\hat{a}$ is a constant value defined as $a/(D-a)$. The field measurement data suggested a linear relationship between $\ln\left(\bar{C}\right)$ and $\ln\left[\hat{a}\left(D-z'\right)/z'\right]$. Examples are shown in Figure 4 at H1303 and H1304 during the neap tidal cycles and at H1305, H1308, X1203, X1204, X1205 and X1207 during the spring tidal cycles. This feature was also true at other measurement sites during the tidal cycles in the CE. We used the slope of $\ln\left(\bar{C}\right)$ to $\ln\left[\hat{a}\left(D-z'\right)/z'\right]$ to set the upper- and lower-bound constraints for the model-computed value of n.

τ_{ce} is explicitly determined via equation (8) in four steps. First, we used the GOCI-retrieved method to estimate the SSC at a depth of 0.5 m. Substituting the GOCI-retrieved SSC into equation (11), we determined the vertical profiles of the SSC at t_1 and configured it as the initial sediment distribution ($C(z)_{t=t_1}$) for the numerical model. Second, we ran the CE-FVCOM sediment model with the inclusion of the horizontal advection, deposition and vertical settling over the period from t_1 to t_2. This allowed us to determine the model-simulated sediment distribution $C_m(z)$ at t_2. During this integration, the erosion term was turned off in the model to avoid the random preset value of τ_{ce}. Third, the vertical profiles of SSC and sediment distribution $C(z)$ at t_2 were determined using the same method as the first step for the GOCI-retrieved SSC. Fourth, the contribution of erosion effect (*Ero*) was determined by the positive difference between $C(z)_{t=t_2}$ and $C_m(z)_{t=t_2}$. Then τ_{ce} can be calculated via equation (8), in which the τ_b was a constant bottom shear stress averaged over the period from t_1 to t_2. This four-step procedure could be repeated for multiple estimations for hourly GOCI images. Since there were a total of 8 GOCI snapshots and if all erosion terms were positive during that period, we could obtain 7 hourly values of τ_{ce}. The final value of τ_{ce} was given by averaging all τ_{ce} values. To guarantee the validity and conservation of the estimated τ_{ce}, we respecified the critical shear stress using this new value and reran the model with an onset of the erosion term to repeat the aforementioned four steps.

Configured with the nonoverlapped unstructured triangular grid, the high-resolution CE-FVCOM provided a better resolution of the geometry of the CE, which featured a multiple channel system with complex

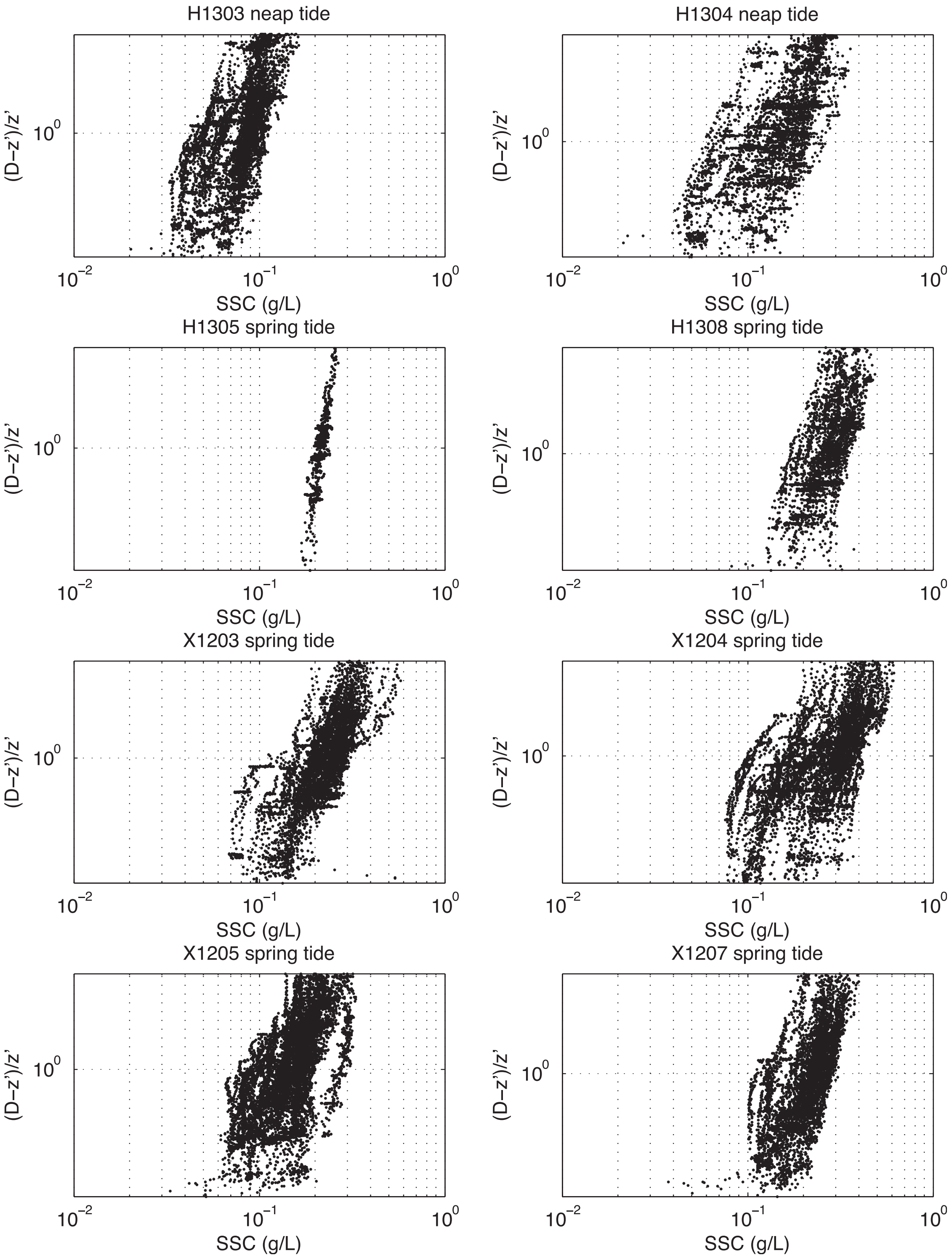

Figure 4. Scatter plots of the *(D-z)/z* via SSC on the natural log plane at selected sites in the Changjiang Estuary.

irregular coastlines and islands [*Chen et al.*, 2006b,; *Xue et al.*, 2009; *Ge et al.*, 2012]. The current version of the CE-FVCOM used in this study was a fully coupled current-wave-sediment system, with an unstructured-grid surface wave model [*Qi et al.*, 2009; *Wu et al.*, 2011] and the sediment model (FVCOM-SED) converted from the USGS community sediment transport model formulation [*Warner et al.*, 2008; *Chen et al.*, 2013]. The FVCOM-SED included the cohesive process of the sediment settling (see Appendix B for details). In the

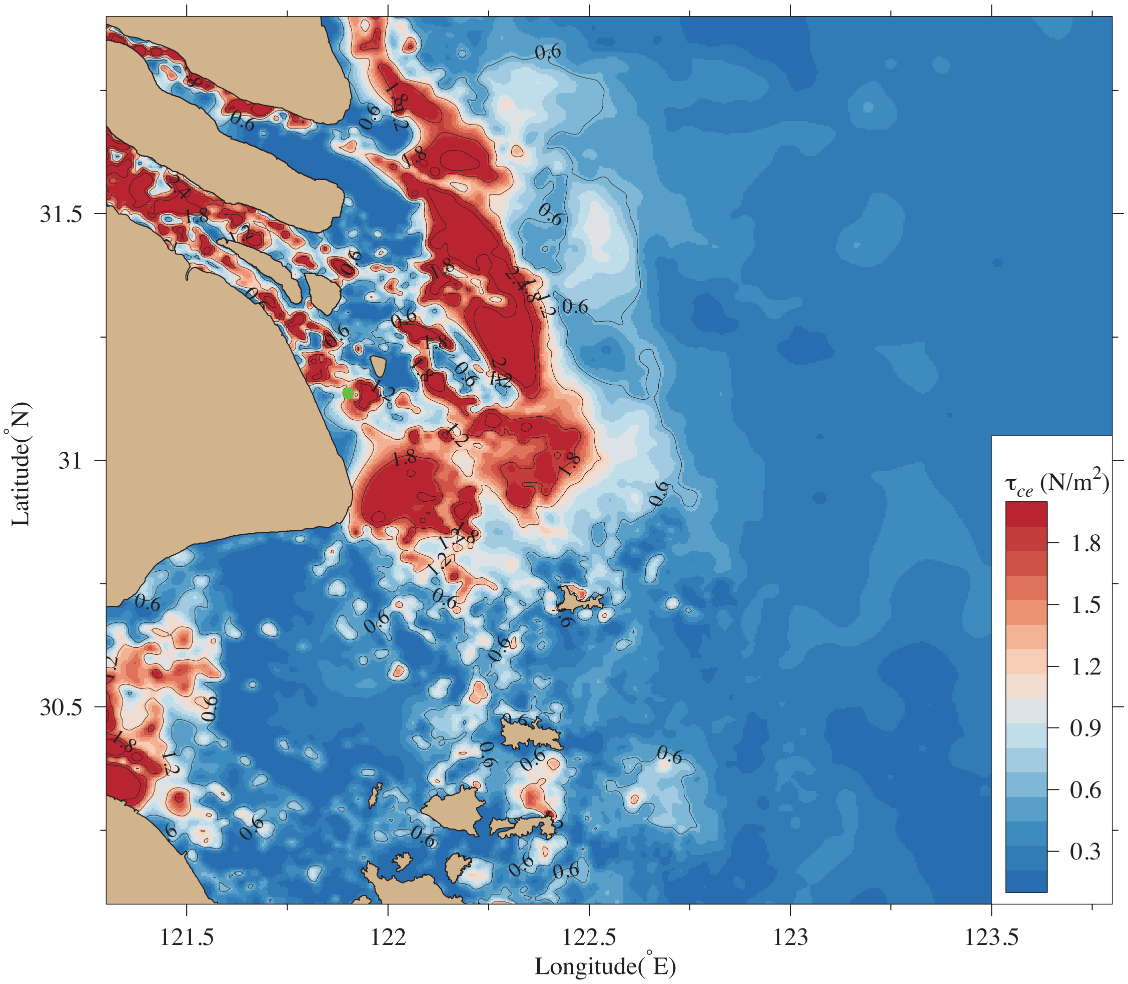

Figure 5. Distribution of the GOCI-retrieved bottom shear stress threshold for erosion (τ_{ce}) in the Changjiang Estuary and Hangzhou Bay. Green bullet in the South Passage indicates the location where the time-varying $\tau_{ce}$was discussed.

CE-FVCOM, τ_b was calculated with the bottom-boundary-layer (BBL) formulation proposed by *Madsen* [1994] and *Styles and Glenn* [2002]. The details of this formulation were described in *Warner et al*. [2008].

The bottom critical shear stress for erosion was estimated over the sediment erosion period during which the GOCI-derived SSC showed a positive change. This produced the time- and spatial-dependent values of τ_{ce} at each model grid over the period during which the GOCI images were selected. The retrieval spatial-dependent mean value of τ_{ce} was given by averaging available estimated samples at individual model grids. The model simulation was then conducted using the time-averaged and spatial-dependent τ_{ce}.

4. Results

4.1. Distributions of τ_{ce}

The estimated τ_{ce} showed a significant spatial-varying pattern in the CE and adjacent coastal region (Figure 5). The amplitude of τ_{ce} in the CE and Hangzhou Bay was in the range of 0.2–3.5 N/m^2. Hangzhou Bay was characterized by a small τ_{ce}, except in the upstream area where the tidal currents were dramatically strong. Since the bottom sediment in this bay was dominated by the fine grain size clay (Figure 3), the suspended sediment concentration was high, even when the wave-current-induced bottom stress was weak. The CE featured a large τ_{ce}, with a mean value of 1.3 N/m^2. The large τ_{ce} generally occurred inside branches, channels, and offshore regions where the tidal flushing was strong or where wind-induced surface waves were energetic. Due to a large river outflow and tidal flushing, a large portion of the fine-size sediment tended to transport seaward. As a result, the sediment in the South Branch and North Channel was dominated by the coarse sands (Figure 3). In contrast, some shallow shoals, such as Jiuduansha, East Hengsha and East Chongming, had a smallτ_{ce}, which explained why the sediment resuspension and shoal-channel sediment exchange were generally larger than other areas during storm events [*Song et al.*, 2013].

There was an exceptional region located around the middle area of the North Passage, North Channel and South Passage where the value of τ_{ce} was comparatively smaller (Figure 5). This was a typical turbidity maximum zone (TMZ) around the mouth of the CE. Since the sediment concentration near the bottom of TMZ was relatively high, the seabed over there was fluffy or even fluidic when local liquefaction occurred over the period of either spring tidal phase or storm events.

Around the 10 m isobath, over the inner shelf off the CE, a relatively high τ_{ce} prevailed in the area with the high clay content. An example can be seen in the outer South Passage and North Branch areas, where the clay content accounted for 20$\sim$45% of the total sediment. In these areas, τ_{ce} could be higher than 1.8 N/m^2. These inner shelf regions were also the major effective areas where surface waves propagated from the ECS, so the wave-current interactions factored significantly in the sediment erosion at the seabed.

4.2. Comparisons With Soil Mechanics Results

Due to difficulties in directly measuring τ_{ce} for erosion in the field, estimations were often made using indirect methods based on soil mechanic theory or laboratory experiments [*Parchure and Mehta*, 1985; *Otsubo and Muraoka*, 1988; *Wilcock*, 1993; *Houwing*, 1999; *Winterwerp and Van Kesteren*, 2004; *Maa et al.*, 2008; *Van Prooijen and Winterwerp*, 2010; *Jacobs et al.*, 2011; *Winterwerp et al.*, 2012]. These estimations were made by relating τ_{ce} to properties of the sediment, such as packing density, particle size, soil structures, cohesiveness, stress history and biological activities [*Partheniades*, 1962; *Panagiotopoulos et al.*, 1997; *Righetti and Lucarelli*, 2007]. A popular empirical expression of τ_{ce} derived with consideration of mud cohesiveness based on soil mechanics [*Smerdon and Beasley*, 1959; *Torfs*, 1995; *Jacobs et al.*, 2011] was given as

$$\tau_{ce}=\gamma_{cr}PI^{\beta} \tag{14}$$

where *PI* (%) is the plasticity index. This plasticity-based formula (hereafter named "PI-method") is valid for the case where $PI >\sim 7\%$, in which the soil primarily exhibits plastic behavior and undergoes a transition from plastic to granular behavior. For the case where $PI < 7\%$, otherwise, the sediment follows the noncohesive sediment dynamics. *Winterwerp et al.* [2012] and *Jacobs et al.* [2011] used this method to estimate τ_{ce}, and their results showed a reasonable match with the estimated values from the observations and laboratory experiments. Using the same parameters of γ_{cr}=0.161 and β=0.8 listed in *Jacobs et al.* [2011], we estimated τ_{ce} based on the sediment properties collected at the measurement sites and compared it with the results calculated by the integrated GOCI-model method.

In the sediment content, *PI* equals the difference between the liquid limit [*LL* (%)] and the plastic limit [*PL* (%)], which varies linearly with the clay content [*Skempton*, 1953] in the form of

$$PI=LL-PL=A(\xi_{cl}-\xi_0) \tag{15}$$

where *A* (−) is the activity of a soil mud; ξ_{cl} (%) is the clay content; and ξ_0 (%) is the onset clay content for cohesive behavior. The activity depends on the clay mineralogy in a variation scale of 0 $\sim$10.

The sediment samples collected at the measurement sites in the CE and Hangzhou Bay during our field surveys were considerably cohesive, with the clay content (consisting of various mud types) being greater than 7% (Figure 3). We measured the water content, plasticity limit, liquid limit, plasticity index and liquid index of these mud samples in the laboratory, and the resulting plasticity index showed a linear relationship with clay content (Figure 6). Most of the valid mud samples had a clay content in the range of 20$\sim$50%, with a squared correlation coefficient of $\sim$0.76, and a mud activity of 0.5. Following the linear relationship between the plasticity index and the clay content, we used equation (14) to estimate the shear stress threshold for erosion based on the in situ sediment data collected at all measurement sites during the four field surveys.

The τ_{ce} values estimated by the PI-method and GOCI-retrieved algorithm at the sediment sampling sites are shown in Figure 7. They all followed the diagnostic line in the scatterplot with a root mean square error of 0.26 N/m^2. There were two regions outside the North Passage and North Branch where the clay content

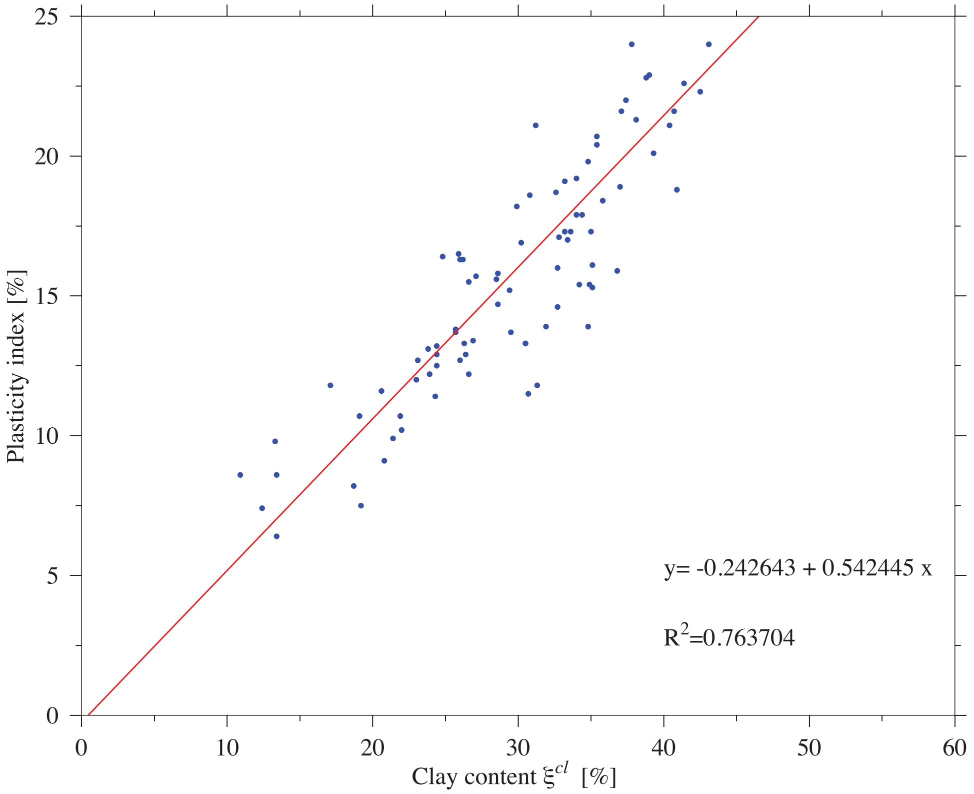

Figure 6. Linear regression between the clay content (ξ_{cl}) of the bed mud and soil plasticity index (*PI*).

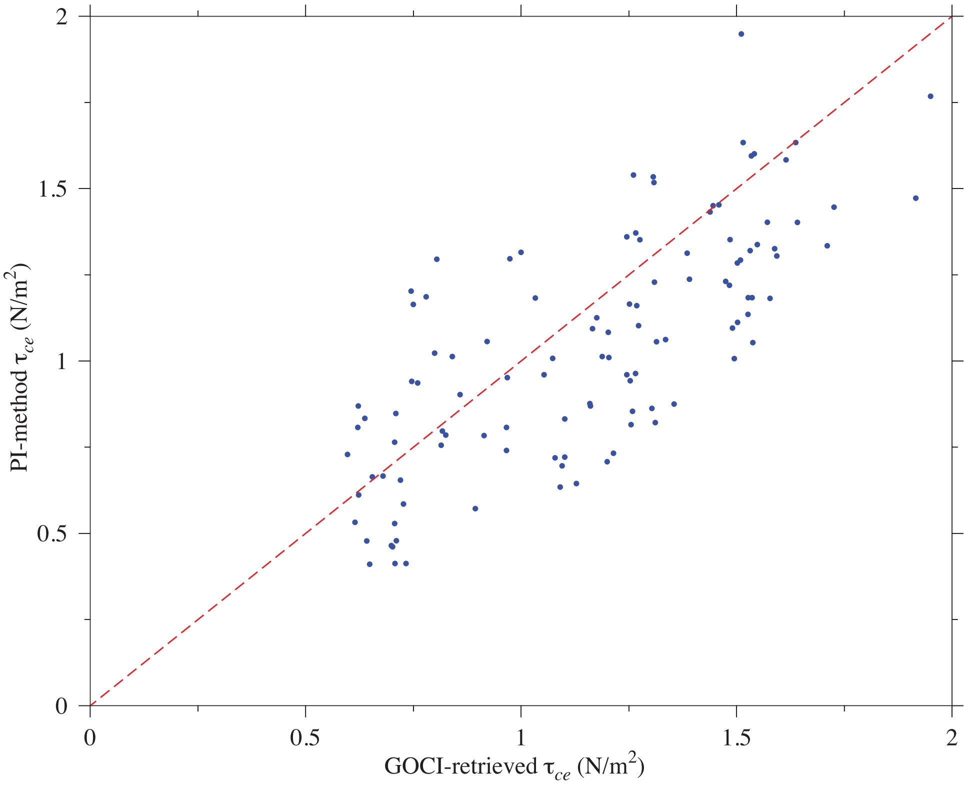

Figure 7. Comparison of the bottom shear stress thresholds for erosion calculated by the PI-method and GOCI-retrieval algorithm.

accounted for 20∼45% of the total sediment. In these two regions, the GOCI-retrieved τ_{ce} was in a range of 1.2∼1.8 N/m^2, which reasonably matched with the value of ∼1.6 N/m^2 estimated using the PI- method.

It should be pointed out that due to the lack of direct measurement data, we could only check to see if the results estimated by the GOCI-retrieved algorithm were consistent with that derived by the PI-method. On the other hand, the good match between the PI-method derived τ_{ce} and the laboratory result suggested that this was a practical method which provided a reasonable estimation ofτ_{ce}. A consistency found in the GOCI-retrieved algorithm and PI-method in our study indirectly demonstrated the capability of using the GOCI satellite data to resolve the spatial pattern of τ_{ce} in the CE and adjacent coastal region.

4.3. Model-Data Comparisons

The main purpose of introducing the GOCI-retrieved algorithm to estimate τ_{ce} was to improve the simulation of the SSC in the CE-FVCOM sediment transport model. We ran the model for two cases in which the bottom critical shear stress for erosion was specified by *a*) a constant value and *b*) spatial-varying values estimated by the GOCI-retrieved algorithm. These two cases covered the period from July to August 2012, during which the field survey was conducted. The results were compared with the observed SSC at the measurement sites shown in Figure 8. A high-resolution measurement array was set around the maximum turbidity zone in the North Passage, from which the water samples were collected at the surface, middle depth and near the bottom during the spring-neap tidal cycles. The SSCs of these samples were measured in the laboratory. For the case with the constant τ_{ce}, to compare with the previous model result from *Song and Wang* [2013], we adopted the same constant value of 0.8 N/m^2, which was used in their paper.

The model-computed SSC for cases *a* and *b* were compared with the observed values at three measurement depths at all survey sites, and an example of the comparison results is shown in Figure 9. Site X1204 was located in the upstream of the South Branch, and sites X1210, CS7S and CS4S were distributed in the North Passage. For the case with spatially nonuniform τ_{ce}, the model-simulated SSC was significantly improved in both low and high turbidity zones (Figure 9). At sites X1204 and X1210, for example, the model-simulated SSC with the GOCI-retrieved τ_{ce} matched well with observations, but it was noticeably underestimated for the case with a spatially uniform τ_{ce}. At site CS7S, the observations showed a significant sediment suspension near the bottom during the maximum turbidity period of 16–19 July 2012. Correspondingly, the maximum SSC of >4.0 g/L appeared near the bottoms of site CS7S. At the site, the SSC was >3.0 g/L at the middle depth. The temporal variability and vertical distribution of the SSC were reasonably resolved for the case with a nonuniform τ_{ce}, but failed to be resolved in the case with a constant τ_{ce}. Similarly, at site CS4S, the observation reported an energetic sediment suspension near the bottom during the same period, with a maximum SSC reaching ∼8 g/L. This pattern was reproduced in case *b*, but not in case *a*. We also made the model-data comparison at all available observation sites for cases *a* and *b*, and the results were consistent with those shown in Figure 9.

The root-mean-square (RMS) errors calculated by the difference of model-simulated and observed SSCs at all available measurement sites for cases *a* and *b* were presented in Table 2. The mean SSC RMS error averaged over 23 sites was 0.79 g/L for case *a* and 0.49 g/L for case *b*, indicating that the model performance improved with a reduction of ∼38% overall simulation error when the spatially nonuniform τ_{ce} was used. Similarly, the mean error for the observed and simulated SSC peak values averaged over all measurement sites, was 1.9 g/L for case a and 0.27 g/L for case b, showing a significant improvement in the case with a spatially nonuniform τ_{ce}.

We also ran the model over a 1 day period during which the GOCI images were collected on 5 April 2011. The spatial distribution of the model-simulated SSC was compared with instantaneous snapshots of the GOCI-derived images taken hourly from 10:16 AM to 03:16 PM. The model-simulated SSC, obtained from case *b* with a spatially nonuniform bottom critical shear stress for erosion, caught the general spatial distribution pattern, which was detected in the GOCI images in the turbidity maximum zones around the mouth of the CE and in Hangzhou Bay (Figure 10). The agreement was also evident in the highly suspended sediment concentration areas over the shallow shoals including Jiuduansha, East Hengsha and the south shoals of Hangzhou Bay. The model also reasonably reproduced the temporal short-term variability of the SSC from 10:16 AM to 03:16 PM, with a notable SSC increase in Hangzhou Bay and a dramatic SSC decrease in the South Passage and North Channel.

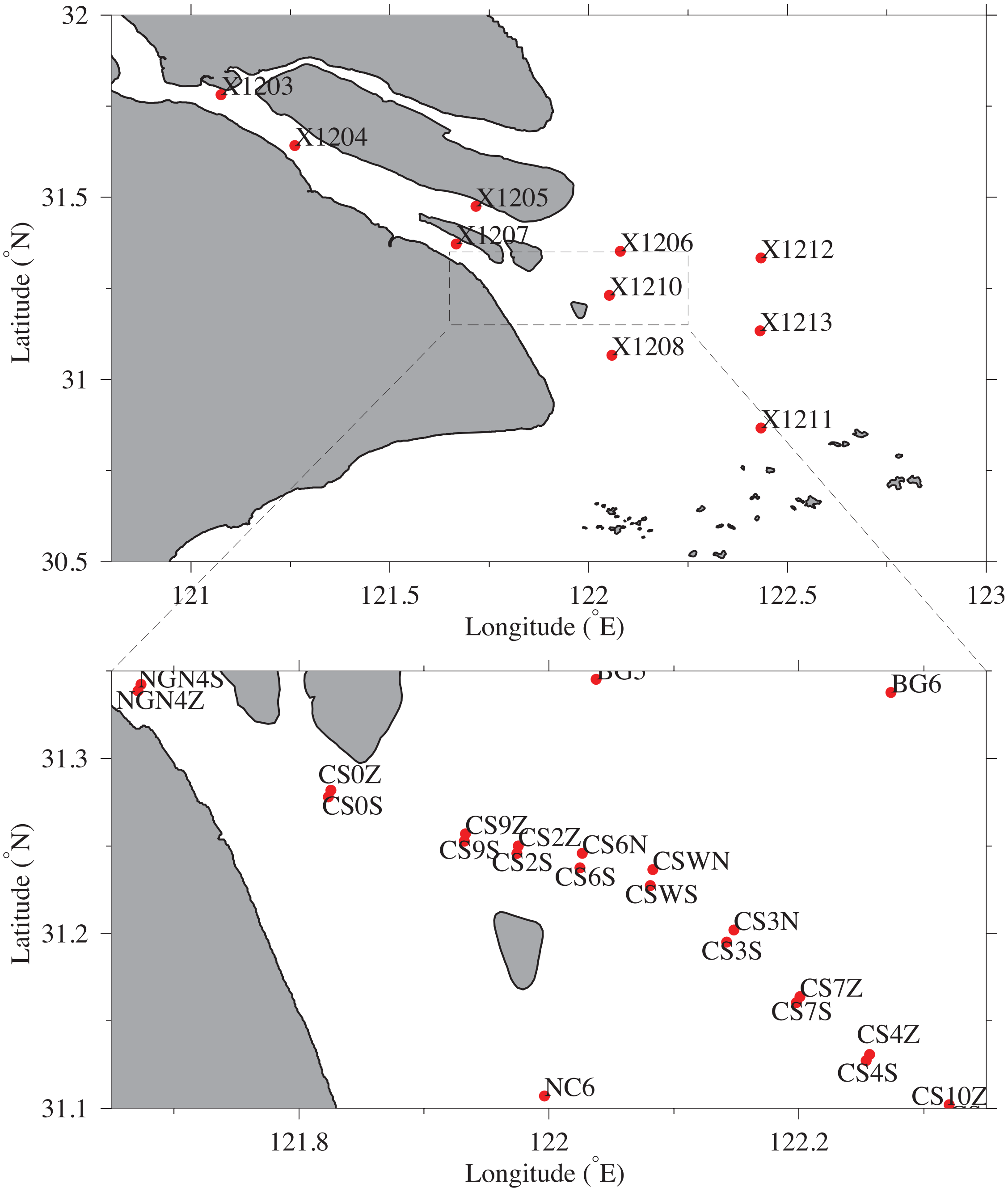

Figure 8. (top) Measurement sites of physical variables and sediment concentration in the Changjiang Estuary. The enlarged view in the bottom plot indicates the locations of high-resolution measurement sites in the North Passage.

We compared the CE-FVCOM-simulated SSC with the previous model-simulated results reported in *Song and Wang* [2013]. The model experiment conducted by *Song and Wang* [2013] was made with a constant τ_{ce}. By tuning τ_{ce}, the model-simulated SSC matched with the observed profile. However, due to the tuning of τ_{ce} at local sites, the model failed to resolve the spatial distribution of the SSC. This was evident in Figures 5 and 9 included in their paper. These two figures showed a low-SSC water environment in the North Passage contrary to observations. We also found that if a constant τ_{ce} was specified, our model showed similar unrealistic results like those of *Song and Wang*'s [2013], suggesting that in order to provide a realistic simulation of the SSC in the CE, one must resolve the spatial distribution of τ_{ce} in that region.

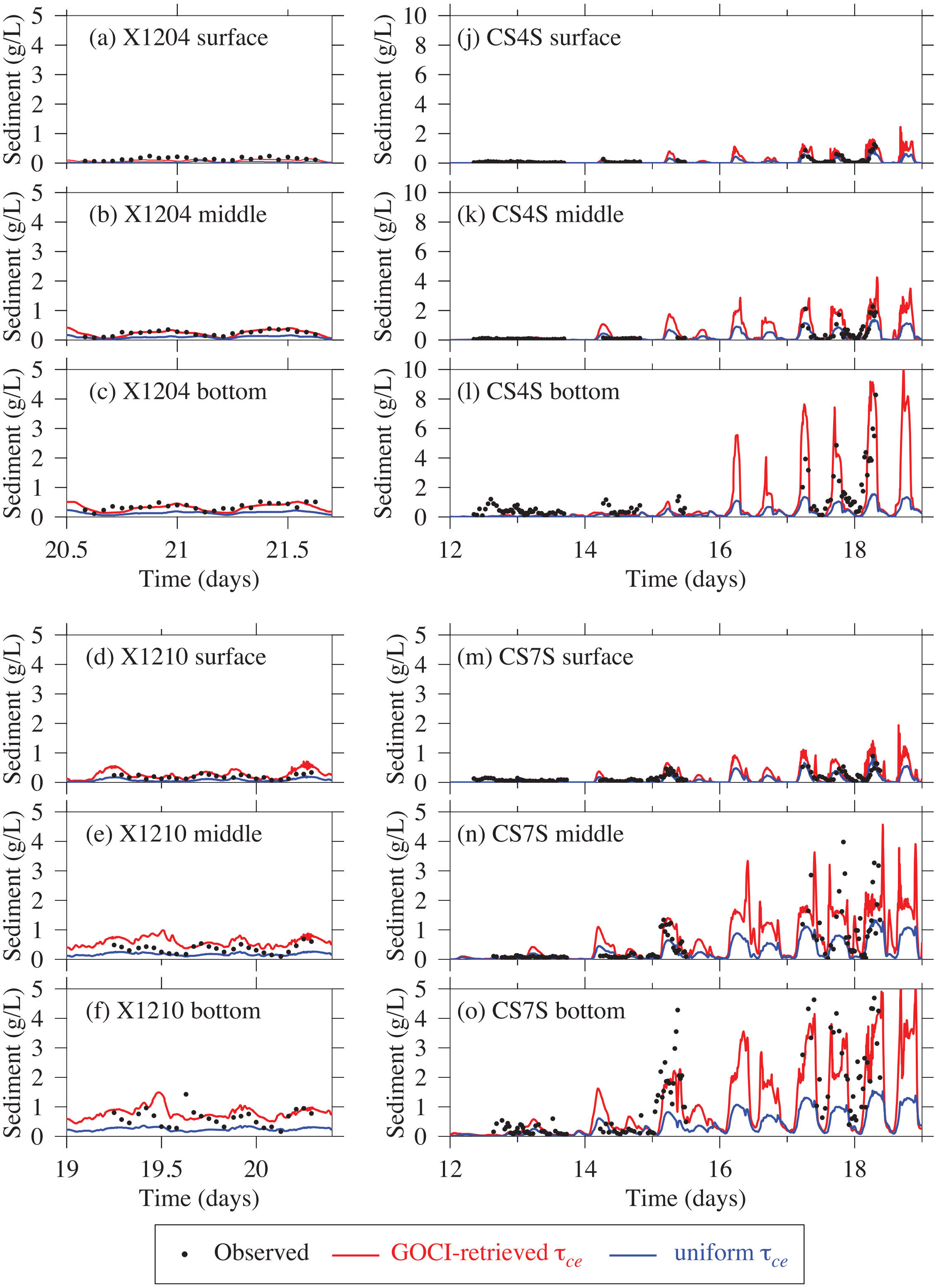

Figure 9. Model-data comparisons of suspended sediment concentration at the surface, middle depth and bottom at measurement sites X1204, X1210, CS3S, CS4S, CS7S, and NGN4S.

4.4. Temporal Variability of Sediment Transport Over the Spring-Neap Tidal Cycle

The model-simulated SSC significantly varied not only over the semidiurnal period but also over the fortnightly spring-neap tidal cycle. We ran the model over the period of March–April 2011 and examined the

Table 2. Root-Mean-Square (RMS) Error and Peak Value Assessment of Numerical Modeling With Constant τ_{ce} and GOCI-Derived Spatially Nonuniform τ_{ce}

	SSC (g/L) RMSE		SSC peak (g/L)		
Station	Uniform τ_{ce}	GOCI-Retrieved τ_{ce}	Observed	Uniform τ_{ce}	GOCI-Retrieved τ_{ce}
CS10Z	0.47	0.35	1.76	0.3	0.29
CS2S	0.53	0.44	1.47	1.03	3.45
CS2Z	1.05	0.86	1.38	0.92	3.07
CS3N	1.14	0.8	5.03	0.93	2.2
CS3S	1.2	0.7	5.28	1.23	2.9
CS3Z	1.2	1.02	4.54	1.27	3.67
CS6N	0.61	0.46	3.11	0.93	4.1
CS6S	0.82	0.55	4.67	1.07	3.96
CS6Z	0.67	0.45	2.45	1.09	4.09
CS7S	0.94	0.72	4.82	1.33	4.03
CS7Z	0.82	0.8	1.1	0.72	1.53
CSWN	1.17	1.0	4.47	1.0	4.39
CSWS	0.81	0.53	7.93	1.41	4.85
CSWZ	1.3	0.86	6.85	1.59	7.79
X1203	0.32	0.15	0.43	0.08	0.49
X1204	0.3	0.18	0.52	0.19	0.47
X1205	0.23	0.12	0.38	0.19	0.37
X1206	0.27	0.15	1.03	0.19	0.46
X1207	0.16	0.14	0.45	0.17	0.21
X1210	0.45	0.33	1.43	0.3	1.44
X1211	0.33	0.25	0.89	0.13	0.35
X1212	0.13	0.13	0.27	0.16	0.17
X1213	0.29	0.17	0.44	0.05	0.21

spatial/temporal variation of the SSC over the spring-neap tidal cycles. The model-simulated SSC was conceptually consistent with the observed distribution of the SSC in the CE and adjacent coastal regions. Figure 11 shows the distributions of the model-simulated SSC at the maximum ebb and flood tides over spring tide cycle from 06:00 PM to 11:00 PM on 4 April 2011. At both the surface and bottom, the model-simulated SSC was high in the estuarine channels where the tidal flow was strong and low over the shoals where the tidal flow was weak. At the maximum ebb tide (Figures11a and 11b), the estuarine water was flushed offshore through multiple deep channels. The SSC was up to $\sim$2.0 g/L near the surface and $\sim$10 g/L near the bottom in the South Passage, North Passage and North Channel, where the maximum turbidity was observed. The suspended sediment transport rate ($\bar{U} \cdot SSC$) also revealed several major seaward transports around the TMZ. The rate over the upstream area and outer shelf out of the TMZ was relatively low. This pattern, however, was quite different in the near-bottom layer (Figure 11b), where a large vertical gradient of SSC was predicted. Both the model and observed results suggested that this gradient was related to water and sediment stratification. Therefore, the suspended sediment flux in the bottom boundary layer accounted for a large portion of the total offshore SSC transport during the ebb tidal period. It was clear that the estuary turbidity maximum regions mainly occurred in the deep channels, separated by shallow shoals like Jiuduansha and Hengsha. At the maximum flood tide (Figures 11c and 11d), however, the strong tidal inflow appeared not only in the channels, but also over the Jiuduansha and Hengsha shoals. This significantly enhanced the lateral sediment exchange between the channels and shoals, resulting in a much broader high-SSC area in the CE throughout the water column. In addition to the vertical erosion process, the horizontal current advection played a role in producing high-SSC areas near the bottom where there was strong tidal current convergence.

The spatial distribution of the SSC over the neap tidal cycle exhibited similar patterns to those over the spring tidal cycle, but the SSC was much lower at both maximum ebb and flood tides (Figure 12). The significant offshore SSC flushing was still evident near the bottom in the main deep channels, but the tidal flow was too weak to bring a significant amount of the sediment from the bottom to the surface. At the maximum ebb tide, the tidal flow was too weak to advect the sediment from the upstream region (Figures 12a and 12b). Similarly, at the maximum flood tide, although the lateral spreading of the inflow still existed, the tidal flow was also relatively weak. At this time, the water exchange between channels and shoals was considerably reduced (Figures 12c and 12d). Near the bottom, the tidal flow was much weaker at the maximum

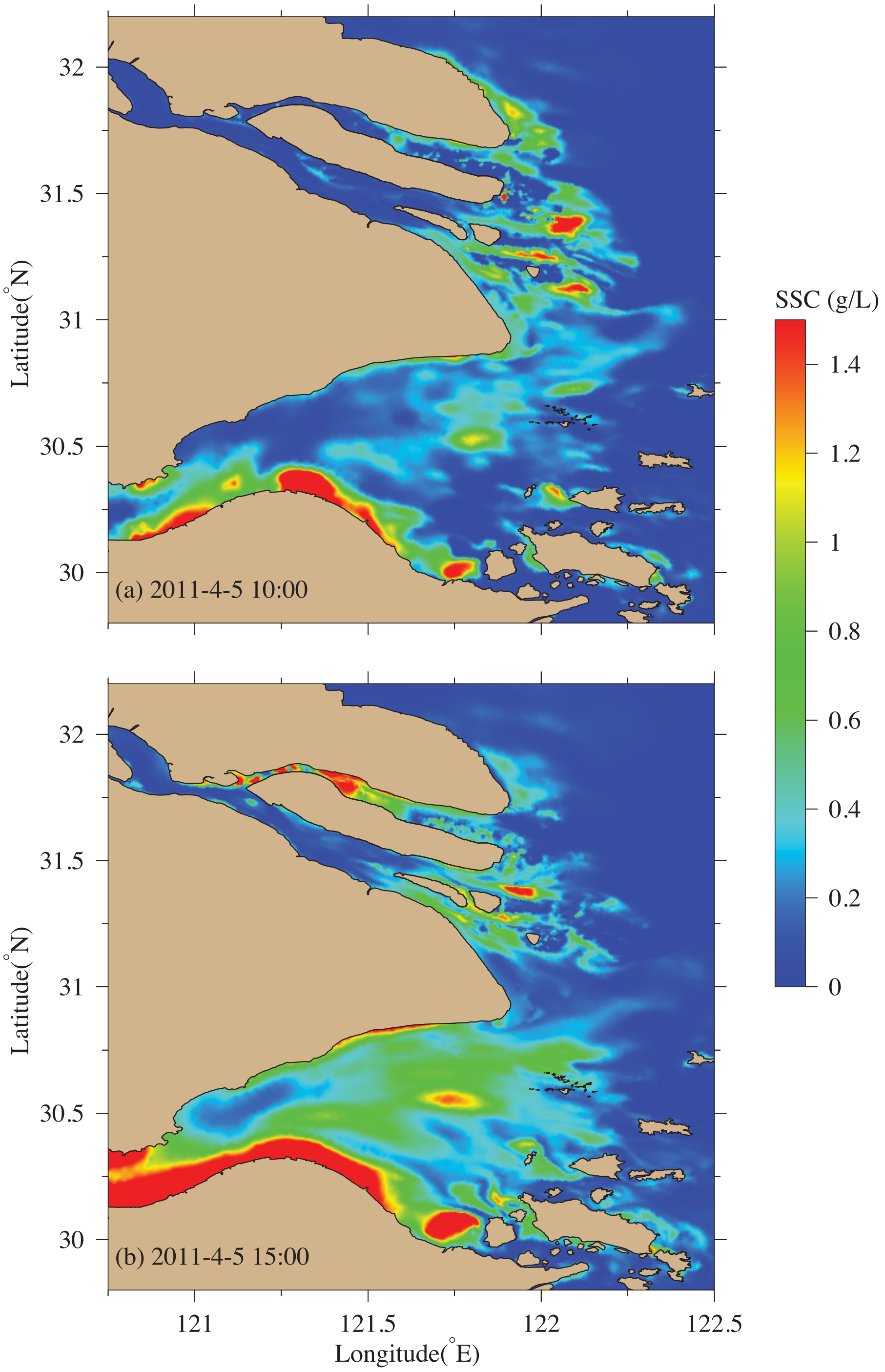

Figure 10. Model-simulated distributions of the surface sediment concentration at (a) 10:00 AM and (b) 03:00 PM on 5 April 2011, respectively.

flood tide than at the maximum ebb tide. As a result, the offshore suspended sediment transport at the maximum ebb tide was larger than the inshore suspended sediment transport at the maximum flood tide.

The model-predicted variability of the SSC over the spring-neap tidal cycle was in agreement with the observational data collected during the field surveys and the GOCI images. This fact convinced us that the model was capable of capturing realistic sediment transport processes in the CE.

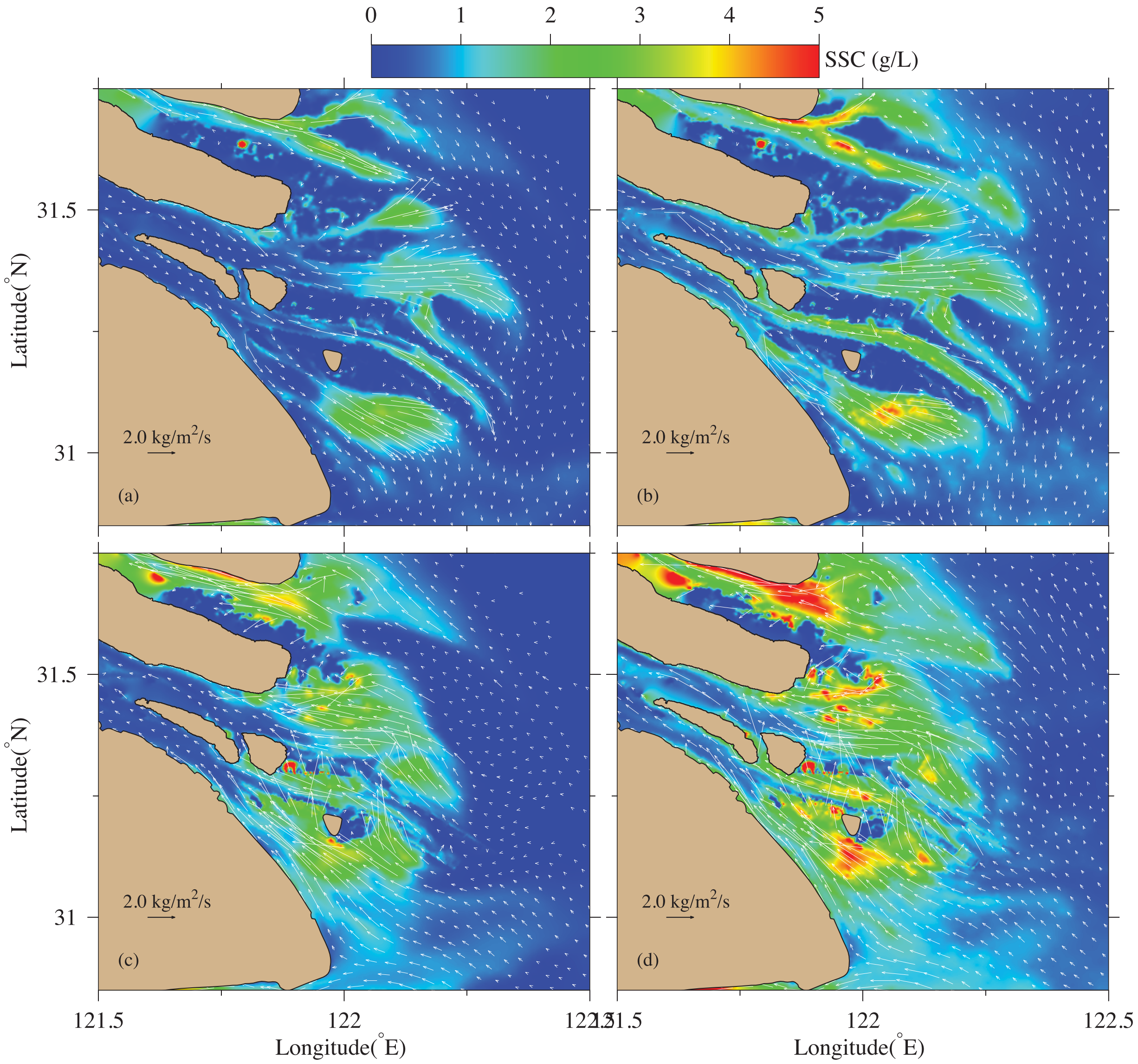

Figure 11. Distributions of (left) surface and (right) bottom suspended sediment concentrations and corresponding sediment transport rate vectors at maximum (top) ebb and (bottom) flood tides during the spring tide at 06:00 PM and 11:00 PM on 4 April 2011, respectively.

5. Discussions

Our studies show that the proposed GOCI-retrieval algorithm for τ_{ce}could significantly improve the model capability of resolving the spatial distribution of the SSC in the CE. Theoretically speaking, the sediment transport includes two physical processes: (1) suspended sediment load and (2) the bedload. In the CE, the suspended sediment was dominated by the local sediment resuspension, with a first-order of magnitude contribution from the local bedload. This was the one of the reasons why the GOCI-retrieval algorithm worked well in our experiments. The sediment dynamics in individual rivers could differ significantly. For an estuary where the local bedload is energetic, the GOCI-retrieval algorithm described in this paper should be modified by including the bedload process. This can be done by adding the bedload component in equation (9).

The profiles of the SSC calculated by the Rouse profile depended on a spatially specified Rouse parameter. This parameter was determined from the observed SSC profiles by the OBS in the field surveys. Previous studies showed that the Rouse parameter could vary over a wide range. It is critical to have sufficient measurements both in space and with time in order to produce a realistic range for this parameter.

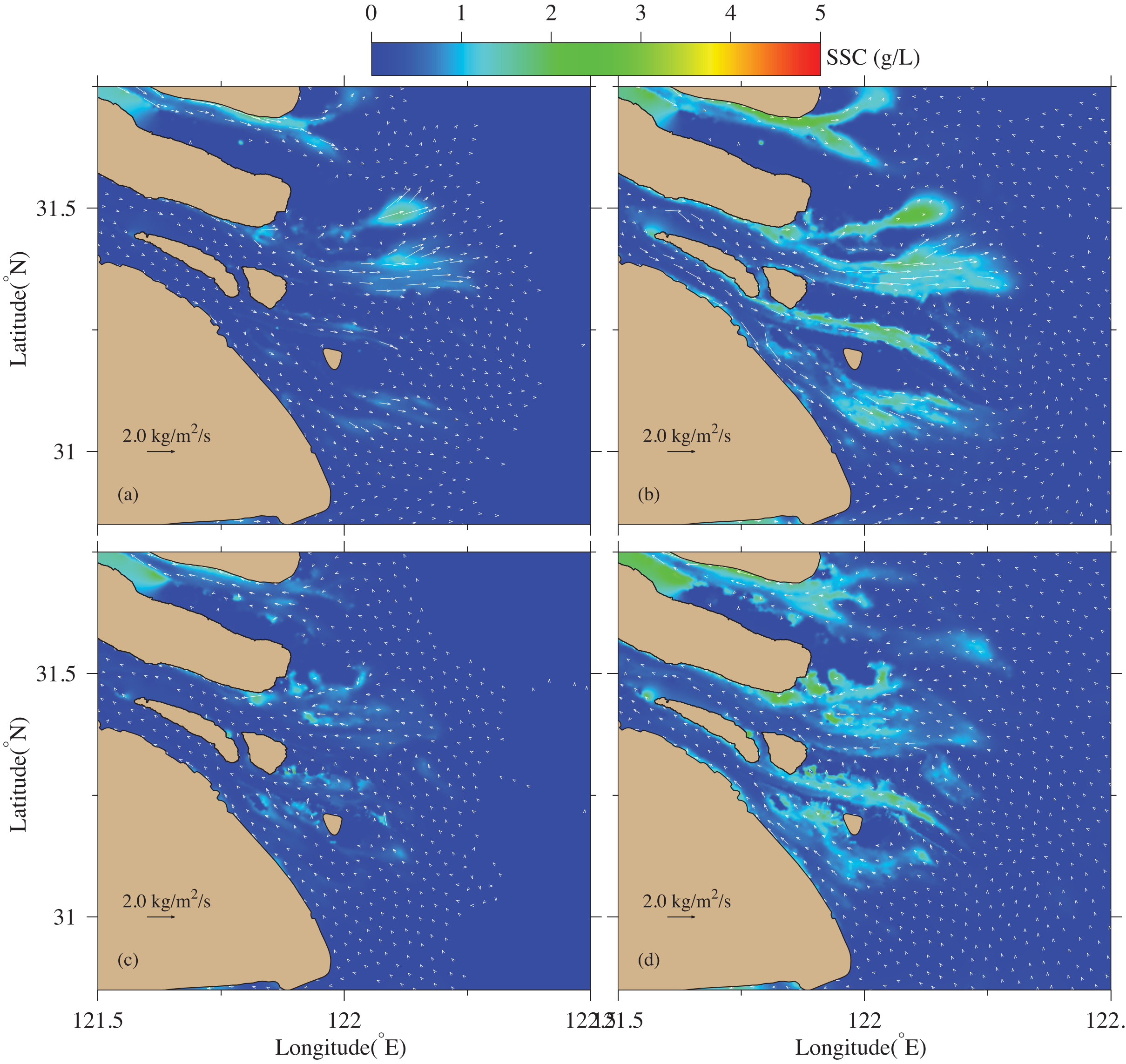

Figure 12. Distributions of (left) surface and (right) bottom suspended sediment concentrations and corresponding sediment transport rate vectors at maximum (top) ebb and (bottom) flood tides during the neap tide at 12:00 AM and 06:00 PM on 12 April 2011, respectively.

To simplify the retrieval algorithm, the erosion rate M, parameterized as a removal capability of soil material from the bed surface due to the current- and turbulence-induced shear stress, was specified as a constant value in previous studies. In fact, this rate depends on bed properties (e.g., bed sediment composition and its consolidation status, etc.) and is controlled by various physical, biological and chemical processes. M is also nonlinearly coupled with the strength of τ_{ce}. To accurately determine the spatial-dependent M, we need more detailed soil mechanic data. These data are especially important in an estuarine turbidity maximum region where the surficial bed sediment features and τ_{ce} could vary with time over tidal cycles. The observations have revealed that, depending on the availability of bed soil, τ_{ce} could be weakened as a result of bottom mud accumulation during the deposition stage and strengthened when the erosion becomes strong. Our algorithm was developed to improve the suspended sediment simulation due to erosion, but we did not consider the decrease of τ_{ce} due to mud accumulation in the surficial bed.

It should be noted that this retrieval algorithm requires an erosion-dominated process. That was the reason why a GOCI data set during the spring tide was selected to estimate τ_{ce} in this paper. We tested this method with other GOCI data sets collected during different spring tidal periods, and the resulting τ_{ce} showed a

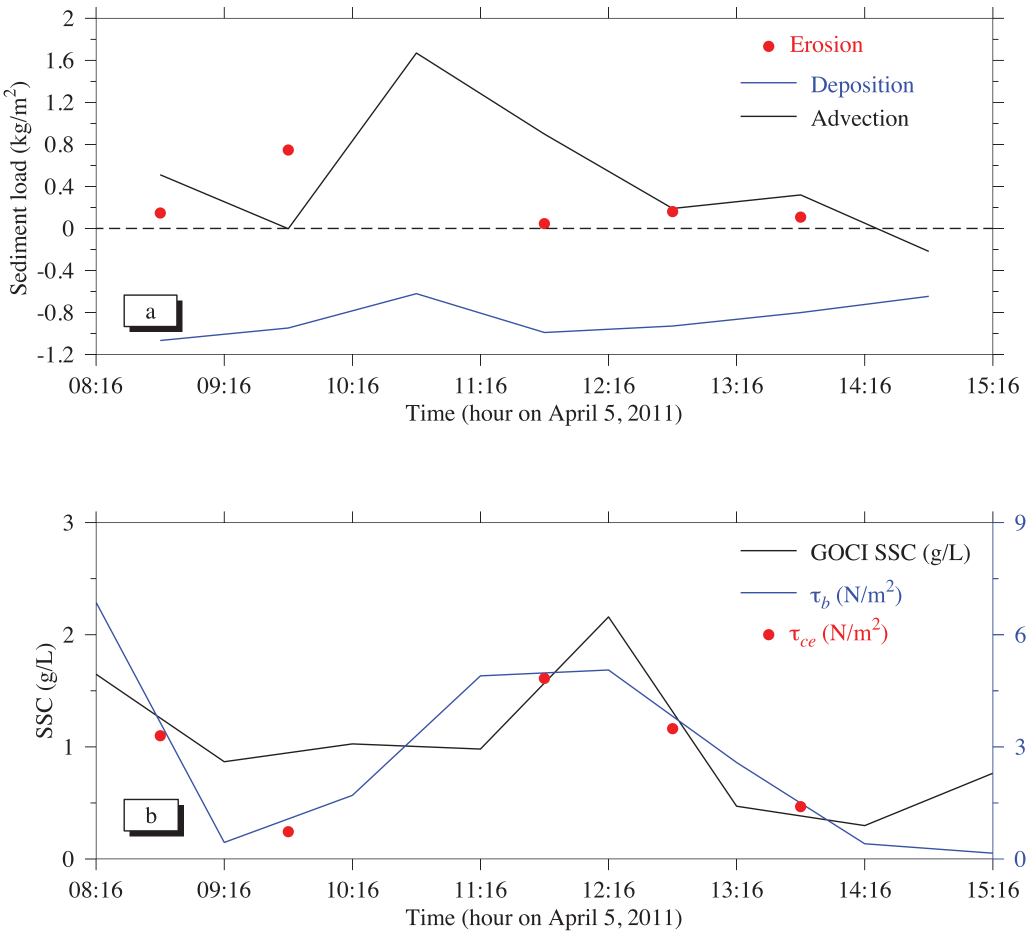

Figure 13. (a) Time series of hourly values of advection (black lines), deposition (blue lines) and erosion (red dots) terms calculated by the CE-FVCOM modeling. (b) Time series of the GOCI-derived near-surface SSC (black lines), near-bottom wave-current-induced shear stress (blue lines) and GOCI-retrieved critical shear stress for erosion (blue dots) at a selected site in the South Passage (green bullet in Figure 5).

similar spatial distribution. The difference was mainly due to the change of bed sediment, tidal currents, and GOCI noise level related to cloud coverage. Applying this method to a neap tidal cycle should be done with caution. During that period, the SSC is generally low (see e.g., Figure 12) and the deposition process could be dominant. The lower SSC in the upper layers exhibits smaller *Ero*, even during an erosion process.

We have also examined the relative scales of the sediment terms at a selected site in the middle of the South Passage near the river mouth (green bullet in Fig. 5). An example is shown in Figure 13a. In our CE-FVCOM experiments, we did not specify the critical shear stress for deposition (τ_{cd}). Therefore, the deposition term produced a relatively stable accumulation of around -1.0 kg/m^2 over hourly intervals at selected sites. The advection term had a similar variation pattern, which was associated with the magnitude and the shear of the model-simulated flow as well as τ_b. It showed that the advection mainly had a positive contribution to the sediment mass at the selected sites during the 8 h period. At the selected sites, compared with the deposition and advection terms, the erosion term, which was determined by equation (9), showed a relatively weaker contribution to the sediment mass of the water column. We did not display the diffusion term in our discussion, because it was one order of magnitude smaller than the other three terms. The variation pattern of the estimated erosion stress threshold at this site is shown in Figure 13b. The surface SSC increased from 09:16 AM to 12:16 PM, during which the tidal current became strong. The results suggested that the increasing of the SSC was mainly controlled by local tidal hydrodynamics. Although the SSC showed a decreasing pattern during the periods of 08:16-09:16 AM and 12:16-02:16 PM, this algorithm produced a positive critical shear stress with a noticeable bottom erosion.

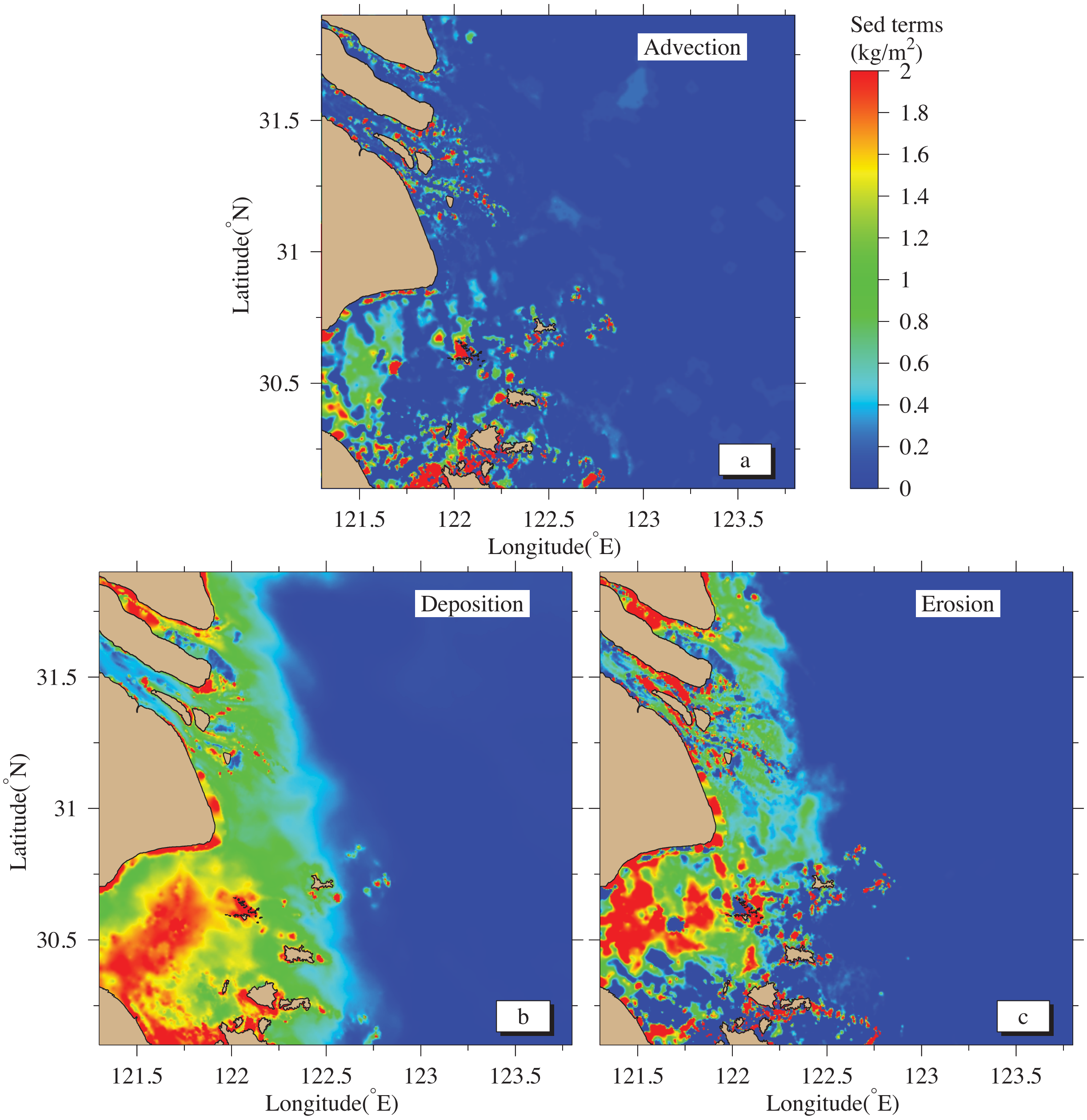

Figure 14. Spatial distributions of time-averaged sediment terms for (a) advection, (b) deposition, and (c) erosion over the experiment period.

Based equation (8), τ_{ce} is mainly determined by the erosion term and τ_b, rather than only the SSC. When τ_b is fixed, a relatively smaller erosion term could lead to a greater τ_{ce} and a larger erosion term, in turn, could lead to a weaker τ_{ce}. This feature, however, did not rely only on the SSC. In our experiments, τ_b varied in space and with time, and was also highly correlated with the advection. The contribution of the advection was either directly or indirectly taken into account. No empirical adjustment was done to tune the erosion term to improve the agreement.

As shown in Figure 13, an inverse relationship was found between the calculated erosion term and the retrieved τ_{ce}. In this case, the erosion term was weaker than the advection and deposition terms. At this selected site, the bed composition was relatively solid, making it difficult to erode under the tide currents.

One should be aware that these findings are only true for the selected sites. At other sites, the magnitudes of advection, deposition and erosion terms could vary significantly due to different bed compositions and tide conditions. Over the experimental period, the time-averaged sediment transport equation showed that the source and sink of the sediment in the CE were mainly balanced between the erosion and deposition processes (Figure 14). During an 8 h simulation period, the advection contribution to the sediment concentration in the water column changed its sign (shown in Figure 13a). Although the tide oscillation did not reach a full cycle within 8 h, the time-averaged advection term was small in most areas, except around some shallow regions in the CE (Figure 14a). The advection term in the middle region of the Hangzhou Bay was relatively higher, which was consistent with the highest SSC zone detected from the GOCI image (Figure 1) and with the stronger tidal currents. The deposition term remained constant relative to the near-bed SSC and matched accordingly with the distribution of the surface SSC (Figure 14b). The estimated erosion term was inversely proportional to τ_{ce} (Figure 5), showing strong erosion in the weak τ_{ce} area and weak erosion in the large τ_{ce} region (Figure 14c).

Finally, using the GOCI-measurement sample fitting to determine the SSC profiles worked well in the CE, but it was limited over the inner shelf of the ECS. In the region where the water depth was deeper than 20 m, the SSC was either low or near a clear water condition. In this circumstance, since the optical reflectance could be mixed with background watercolor signals, the GOCI-revealed SSC was low (eg. $<$10 mg/L). The resuspended load and related erosion load from the algorithm could be small, limiting the retrieval precision for τ_{ce}. Therefore, caution should be paid when using the GOCI-retrieval algorithm to estimate the bottom critical shear stress for erosion in low turbidity water regions.

6. Summaries and Conclusions

A new method, which integrates the GOCI satellite observations, soil mechanic sampling and numerical modeling, was developed with an aim to estimate the spatial variation of the bottom critical shear stress for erosion in the high-turbidity CE and adjacent coastal regions. The retrieval procedure was applied to calculate the bottom shear stress threshold for erosion, with consideration for the cohesive mud and mud-sand mixture, and the resulting stress was compared with that estimated by the traditional soil mechanics theory and validated by evaluating the degree of the improvement in the SSC simulation.

The values of the bottom critical shear stress estimated by the PI-method and GOCI-retrieved algorithm exhibited the same pattern, which was also consistent with the clay content. The high-resolution sediment transport model with an implementation of the GOCI-derived τ_{ce} significantly improved the SSC simulation in the turbidity maximum region in the CE and Hangzhou Bay. The model has also reproduced the temporal variability of the SSC not only over the short-term semidiurnal scale but also over the fortnightly spring-neap tidal cycles. The results suggested that a significant lateral water exchange between channels and shoals occurred during the spring flood tide, leading to a broader high-SSC area throughout the water column in the CE.

In this study, the estimation of the bottom critical shear stress for erosion was made by combining the hourly GOCI images, soil mechanics and numerical modeling. The accuracy of the estimated τ_{ce} was limited by the spatial and temporal resolutions of the satellite images, the accuracy of the semiempirical radiative transfer algorithm to retrieve the surface SSC from the images, the correctness of the soil mechanics theory, and the capability of the numerical model to resolve fluid hydrodynamics. Several steps could ensure the accuracy of the estimation. First, a careful calibration of the retrieval algorithm for satellite images should be done to verify the correctness of this method over a wide range of sediment concentrations. Second, sufficient water samples in different types of sediment zones should be collected to compare the results with observations. Third, a high-resolution sediment transport model should be used to resolve realistic spatial varying bathymetry and bed composition in the CE.

Finally, it should be pointed out that the GOCI-retrieval algorithm was developed to improve the simulation for the erosion-dominant spatial structure and temporal variability of the SSC in the high-turbidity CE. The approach described in this paper provided us with an alternative method to resolve the spatial structure of the bottom critical shear stress for erosion. Direct application of this method to other estuaries should be done with caution, given the limitation of the GOCI-image accuracy in the low-SSC area and the lack of the bedload process. These two factors have not been taken into account in this study. Modifications could be made following the same approach described in this paper.

Appendix A: Derivation of Sediment Terms

According to the governing equation of the three dimensional suspended sediment transport, the sediment content and local change at the given location and time could be given as

$$\frac{\partial C}{\partial t}+\nabla_H\cdot(\boldsymbol{u}C)+\frac{\partial(\omega-\omega_s)C}{\partial z}=\frac{\partial}{\partial z}\left(K_M\frac{\partial C}{\partial z}\right) \tag{A1}$$

where ∇_H represents the horizontal derivative, C (g/L) is the concentration of the suspended sediment; K_M (m^2/s) is the vertical eddy viscosity; ω_s (m/s) and w (m/s) are the vertical sediment-settling and water velocities, respectively; and $\boldsymbol{u}$ (m/s) is the horizontal water velocity vector. The diffusion term is generally orders of magnitude smaller compared with advection, erosion, deposition, and settling, and is therefore omitted in this study.

Depth-integrating the equation (A1) yields

$$\begin{aligned}\frac{\partial}{\partial t}\int_{-h}^{\zeta}Cdz-C(\zeta)\frac{\partial\zeta}{\partial t}+\nabla_H\cdot\int_{-h}^{\zeta}Cudz-C(\zeta)\nabla_H\cdot u(\zeta)+C(-h)\nabla_H h\cdot u(-h)\\+C(\zeta)\omega(\zeta)-C(-h)\omega(-h)+C(\zeta)\omega_s(\zeta)-C(-h)\omega_s(-h)\\=K_M\frac{\partial C}{\partial z}\bigg|_{\zeta}-K_M\frac{\partial C}{\partial z}\end{aligned} \tag{A2}$$

where h is the water depth and ζ is the water surface elevation. Using the surface and bottom boundary conditions

$$\frac{\partial\zeta}{\partial t}+\nabla_H\zeta\cdot u(\zeta)-\omega(\zeta)=0,\quad z=\zeta \tag{A3}$$

$$\nabla_H h\cdot u(-h)-\omega(-h)=0,\quad z=-h \tag{A4}$$

$$K_M\frac{\partial C}{\partial z}\bigg|_{\zeta}=0,\quad z=\zeta \tag{A5}$$

and assuming

$$C(\zeta)\omega_s(\zeta)=0, \tag{A6}$$

then equation (A4) becomes

$$\frac{\partial}{\partial t}\int_{-h}^{\zeta}Cdz+\nabla_H\cdot\int_{-h}^{\zeta}C\boldsymbol{u}dz=-K_M\frac{\partial C}{\partial z}\bigg|_{-h}+C(-h)\omega(-h). \tag{A7}$$

The right-hand terms can be expressed as the source and sink terms of the erosion and deposition rates, that is

$$\frac{\partial}{\partial t}\int_{-h}^{\zeta}Cdz+\nabla_H\cdot\int_{-h}^{\zeta}C\boldsymbol{u}dz=-D+E \tag{A8}$$

where D and E represent the deposition and erosion rates, respectively. Integrating (A8) over the period from t_1 to t_2, we have

$$\int_{t_1}^{t_2}Edt=\int_{-h}^{\zeta(t_2)}C(t_2)dz-\int_{-h}^{\zeta(t_1)}C(t_1)dz+\int_{t_1}^{t_2}\left(\nabla_H\cdot\int_{-h}^{\zeta}C\boldsymbol{u}dz\right)dt+\int_{t_1}^{t_2}Ddt. \tag{A9}$$

In equation (A9), $\int_{t_1}^{t_2}Edt$ is the erosion term (*Ero*), $\int_{t_1}^{t_2}\left(\nabla_H\cdot\int_{-h}^{\zeta}C\boldsymbol{u}dz\right)dt$ is the contribution of advection term (*Adv*) and $\int_{t_1}^{t_2}Ddt$ indicates the deposition term (*Dep*).

Appendix B: The CE-FVCOM Sediment Transport Model

The CE-FVCOM was described in *Ge et al*. [2013] and a brief description of the sediment model is given here. The computational domain covered the CE and its adjacent bay and shelf regions, with a spatial resolution up to 200 m in the main channels and passages [see *Ge et al*., 2013, Figure 5]. In the FVCOM sediment transport model, the sediment composition was divided into multiple sediment groups based on the sediment median grain size [*Chen et al*., 2013]. The governing equation of the suspended sediment concentration of the *i*th sediment group in the water column was given as

$$\frac{\partial C_i}{\partial t}+\frac{\partial uC_i}{\partial x}+\frac{\partial vC_i}{\partial y}+\frac{\partial (w-w_i)C_i}{\partial z}=\frac{\partial}{\partial x}\left(A_H\frac{\partial C_i}{\partial x}\right)+\frac{\partial}{\partial y}\left(A_H\frac{\partial C_i}{\partial y}\right)+\frac{\partial}{\partial z}\left(K_M\frac{\partial C_i}{\partial z}\right) \tag{A10}$$

where C_i (g/L) is the concentration of the individual sediment group and w_i (m/s) is the settling velocity. In this study, we only considered one single group with median particle class of suspended sediment.

The boundary condition at the sea surface and water-bed bottom were given as

$$\left(K_M\frac{\partial C_i}{\partial z}\right)=0,\ \ at\ \ z=\zeta, \tag{A11}$$

$$\left(K_M\frac{\partial C_i}{\partial z}\right)=ERO_i-DEP_i,\ \ at\ \ z=-H. \tag{A12}$$

Specifying w_i was much more complex than that of the sand due to the flocculation process of particle aggregation associated with the sediment concentration, turbulent strength of the flow, sediment characteristics, etc. [*Soulsby et al*., 2013]. Various flocculation models were used to set w_i, which involved different parameter combinations of the sediment and turbulent flow [*Van Leussen*, 1994; *Winterwerp*, 1999; *Whitehouse et al*., 2000; *Winterwerp et al*., 2006; *Verney et al*., 2011; *Lee et al*., 2011]. We also took the flocculation into account by using *Soulsby et al*. [2013] to calculate w_i in the CE. Two groups of flocs, macroflocs in a size range of 160–500 μm and microflocs in a size range of 20–160 μm, were considered. Here w_i was defined as the weight averaged value of settling velocities of macroflcs (w_{sM}) and microflocs ($w_{s\mu}$) and is given as

$$w_i=\max\left[rw_{sM}+(1-r)w_{s\mu},0.2\times 10^{-3}\right] \tag{A13}$$

where r is the proportion of the total mass of suspended particulate matter (SPM) (mg/L) of macroflocs, specified as

$$r=\begin{cases} 0.1 & X<0 \\ 0.1+0.221X & for\ 0\le X<4.07 \\ 1 & X\ge 4.07 \end{cases} \tag{A14}$$

in which $X=log_{10}c+6$, and $c=SPM/\rho$ is the dimensionless concentration.

The macrofloc and microfloc settling velocities are calculated as:

$$w_{sM}=0.595\left(\frac{u_*^3\xi\bar{d}_\mu^4}{\upsilon^3 z}\right)^{0.166}gc^{0.22044}\left(\frac{vz}{u_*^3\xi}\right)^{1/2}\exp\left[-\left(\frac{u_{*sM}}{u_*\xi^{1/2}}\right)^{0.463}\right] \tag{A15}$$

$$w_{s\mu}=0.5372\left(\frac{u_*^3\xi\bar{d}_\mu^4}{\upsilon^3 z}\right)^{0.39}g\left(\frac{vz}{u_*^3\xi}\right)^{1/2}\exp\left[-\left(\frac{u_{*s\mu}}{u_*\xi^{1/2}}\right)^{0.66}\right] \tag{A16}$$

where g is the gravity acceleration rate; $d_\mu=10^{-4}$ m; $d_1=10^{-5}$ m;$u_{*sM}=0.067$ m s^{-1}; $u_{*s\mu}=0.025$ m s^{-1}; $\xi=1-z/h$; and v is the kinematic viscosity of the water. We set a minimum value of $w_{s,av}=0.2$ mm s^{-1} to avoid the shutdown of the settling velocity for the case in which either tightly bound microflocs were too small or $u_*=0$ (no flow) at $z=0$ (sea bed) or $\xi=0$. Recent observations in the CE revealed that the mean diameters of in situ flocs were in a range of ~50–120 μm, whereas the median dispersed grain size was about 7–11 μm [*Guo and He*, 2011]. This evidence indicated that the microflocs dominated the floc contents in our study region.

It should be noted that the settling velocity calculated in equation (A13) may be underestimated in the region with the high sediment concentration [*Winterwerp and Van Kesteren*, 2004]. This happened near the river mouth of the CE, particularly in the North and South Passages where the water was strongly stratified. We considered this factor by including the hindered settling under the high sediment concentrated water defined as

$$w_i=\frac{(1-\phi_f)(1-\phi_s)}{1+2.5\phi_f}w_0 \tag{A17}$$

where $\phi_s=c/\rho_s$ is the overall volumetric concentration and $\phi_f=c/c_{gel}$ is the flocculation volumetric concentration; c is the instantaneous sediment concentration; c_{gel} is the gelling concentration (specified as 250 g/L in this study); and ρ_s is the sediment density.

The CE-FVCOM was run over the period of March–April 2011 and July–August 2012, respectively. It was driven by the WRF-produced meteorological forcing at the surface [*Ge et al*., 2013], the daily freshwater discharge with an average SSC load of 0.3 g/L at the upstream end [*Hu et al*., 2009], and tidal forcing consisting of eight major astronomical tidal constituents (M_2, S_2, K_2, N_2, K_1, O_1, P_1, and Q_1) at the open boundary over the shelf. The temperature and salinity were initialized using the March and July climatological field respectively, and the SSC in the water column was specified to be zero at initial. On the open boundary, the temperature and salinity were specified by the regional ECS-FVCOM output through the one-way nesting [*Ge et al*., 2015].

The hydrodynamic component of CE-FVCOM was validated by comparing the observed tidal elevation/currents, salinity and significant wave heights/peak periods in the real-time simulation experiments [*Ge et al*., 2012, 2013]. In this study, the CE-FVCOM was run for a period from 20 March to 13 April 2011. The model-simulated physical variables on 5 April 2011 were used to estimate the critical shear stress for erosion.

Acknowledgments
This work is supported by the National Science Foundation of China (grants 41306080; 41271375; 51320105005), and the Public Service Program of State Ocean Administration (contract 201205017-2), and the SKELC independent fund (2011RCDW03). Changsheng Chen's participation was supported by the International Center for Marine Studies, Shanghai Ocean University and the Zijiang Scholar Program at State Key Laboratory of Estuarine and Coastal Research (SKLEC), the East China Normal University (ECNU) . The GOCI images were provided by the Korea Ocean Satellite Center (http://kosc.kiost.ac/kosc_web/GOCI_do-wnload/SatelliteData.html). The data of seabed samples collected at several mooring stations in August 2012 (Figure 8, bottom) were kindly provided by the Yangtze Estuary Waterway Administration Bureau, Ministry of Communication, Shanghai. The water sample data collected at the moorings (X1203-X1213) in 2011 and 2013, 2014 surveys were obtained by our own field surveys. These data will be made available upon request to Jianzhong Ge (Email: jzge@sklec.ecnu.edu.cn). The efforts of our researchers and students in the SKLEC/ECNU who participated in the field surveys are sincerely appreciated. The authors also greatly appreciate two anonymous reviewers and Fengyan Shi at the University of Delaware for their valuable comments and suggestions.

References

Amos, C. L., G. Umgiesser, C. Ferrarin, C. E. L. Thompson, R. J. S. Whitehouse, T. F. Sutherland, and A. Bergamasco (2010), The erosion rates of cohesive sediments in Venice lagoon, Italy, *Cont. Shelf Res.*, *30*(8), 859–870, doi:10.1016/j.csr.2009.12.001.

Amoudry, L. O., and A. J. Souza (2011), Deterministic coastal morphological and sediment transport modeling: A review and discussion, *Rev. Geophys.*, *49*, RG2002, doi:10.1029/2010RG000341.

Andersen, T. J., J. Fredsoe, and M. Pejrup (2007), In situ estimation of erosion and deposition thresholds by Acoustic Doppler Velocimeter (ADV), *Estuarine Coastal Shelf Sci.*, *75*(3), 327–336, doi:10.1016/j.ecss.2007.04.039.

Ariathurai, C. R., and K. Arulanandan (1978), Erosion rates of cohesive soils, *J. Hydraul. Div. Am. Soc. Civ. Eng.*, *104*(2), 279–282.

Carniello, L., A. Defina, and L. D'Alpaos (2012), Modeling sand-mud transport induced by tidal currents and wind waves in shallow microtidal basins: Application to the Venice Lagoon (Italy), *Estuarine Coastal Shelf Sci.*, *102-103*, 105–115, doi:10.1016/j.ecss.2012.03.016.

Chao, X., Y. Jia, F. D. Shields Jr., S. S. Y. Wang, and C. M. Cooper (2008), Three-dimensional numerical modeling of cohesive sediment transport and wind wave impact in a shallow oxbow lake, *Adv. Water Resour.*, *31*(7), 1004–1014, doi:10.1016/j.advwatres.2008.04.005.

Chen, C., J. Zhu, R. C. Beardsley, and P. J. S. Franks (2003), Physical-biological sources for dense algal blooms near the Changjiang River, *Geophys. Res. Lett.*, *30*(10), 1515, doi:10.1029/2002GL016391.

Chen, C., L. Wang, R. Ji, J. W. Budd, D. J. Schwab, D. Beletsky, G. L. Fahnenstiel, H. A. Vanderploeg, B. J. Eadie, and J. Cotner (2004), Impacts of suspended sediment on the ecosystem in Lake Michigan: A comparison between the 1998 and 1999 plume events, *J. Geophys. Res. 109*, C10S05, doi:10.1029/2002JC001687.

Chen, C., R. C. Beardsley, and G. Cowles (2006b), An unstructured grid, finite-volume coastal ocean model (FVCOM) system, *Oceanography*, *19*(1), 78–89.

Chen, C., et al. (2013), An unstructured grid, finite-volume community ocean model FVCOM user manual, *SMAST/UMASSD-13-0701*, New Bedford, Mass. [Available at http://fvcom.smast.umassd.edu/fvcom/.]

Chen, J., D. Li, B. Chen, F. Hu, H. Zhu, and C. Liu (1999), The processes of dynamic sedimentation in the Changjiang Estuary, *J. Sea Res.*, *41*(1-2), 129–140.

Chen, S. L., G. A. Zhang, S. Y. Yang, and J. Z. Shi (2006a), Temporal variations of fine suspended sediment concentration in the Changjiang River estuary and adjacent coastal waters, China, *J. Hydrol.*, *331*(1-2), 137–145, doi:10.1016/j.jhydrol.2006.05.013.

Cho S., Y. H. Ahn, J. H. Ryu, G. S. Kang, and H. S. Youn (2010), Development of Geostationary Ocean Color Imager (GOCI), *Korean J. Remote Sens.*, *26*(2), 157–165.

Choi, J. K., Y. J. Park, J. H. Ahn, H. S. Lim, J. Eom, and J. H. Ryu (2012), GOCI, the world's first geostationary ocean color observation satellite, for the monitoring of temporal variability in coastal water turbidity, *J. Geophys. Res.*, *117*, C09004, doi:10.1029/2012JC008046.

de Linares, M., and P. Belleudy (2007), Critical shear stress of bimodal sediment in sand-gravel rivers, *J. Hydraul. Eng.*, *133*(5), 555–559, doi:10.1061/(ASCE)0733-9429(2007)133:5(555).

Deltares (2012), *User manual for Delft3d-Flow Simulation of Multi-Dimensional Hydrodynamic Flows and Transport Phenomena, Including Sediments*, Netherlands, Delft.

Doerffer, R., and H. Schiller (2007), The MERIS case 2 water algorithm, *Int. J. Remote Sens.*, *28*, 517–535.

Doerffer, R., and H. Schiller (2008), *MERIS Regional Coastal and Lake Case 2 Water Project—Atmospheric Correction ATBD*, version 1.0, GKSS Res. Cent. Geesthacht, Germany.

Doxaran, D., J. M. Froidefond, S. Lavender, and P. Castaing (2002), Spectral signature of highly turbid waters: Application with SPOT data to quantify suspended particulate matter concentrations, *Remote Sens. Environ.*, *81*, 149–161.

Doxaran, D., J. M. Froidefond, P. Castaing, and M. Babin (2009), Dynamics of the turbidity maximum zone in a macrotidal estuary (the Gironde, France): Observations from field and MODIS satellite data, *Estuarine Coastal Shelf Sci.*, *81*, 321–332.

Du, P., P. Ding, and K. Hu (2010), Simulation of three-dimensional cohesive sediment transport in Hangzhou Bay, China, *Acta Oceanol. Sin.*, *29*(2), 98–106, doi:10.1007/s13131-010-0028-9.

Ge, J., C. Chen, J. Qi, P. Ding, and R. C. Beardsley (2012), A dike–groyne algorithm in a terrain-following coordinate ocean model (FVCOM): Development, validation and application, *Ocean Modell.*, *47*, 26–40, doi:10.1016/j.ocemod.2012.01.006.

Ge, J., P. Ding, C. Chen, S. Hu, G. Fu, and L. Wu (2013), An integrated East China Sea–Changjiang Estuary model system with aim at resolving multi-scale regional–shelf–estuarine dynamics, *Ocean Dyn.*, *63*(8), 881–900, doi:10.1007/s10236-013-0631-3.

Ge, J., P. Ding, and C. Chen (2015), Low-salinity plume detachment under non-uniform summer wind off the Changjiang Estuary, *Estuarine Coastal Shelf Sci.*, *156*, 61–70, doi:10.1016/j.ecss.2014.10.012.

Grabowski, R. C., G. Wharton, G. R. Davies, and I. G. Droppo (2012), Spatial and temporal variations in the erosion threshold of fine riverbed sediments, *J. Soils Sediments*, *12*(7), 1174–1188, doi:10.1007/s11368-012-0534-9.

Guo, L., and Q. He (2011), Freshwater flocculation of suspended sediments in the Yangtze River, China, *Ocean Dyn.*, *61*(2), 371–386, doi: 10.1007/s10236-011-0391-x.

Hamrick, J. M. (1992a), A three-dimensional environmental fluid dynamics computer code: Theoretical and computational aspects, *Spec. Rep. 317*, 63 pp., Coll. of William and Mary, Va. Inst. of Mar. Sci., Gloucester Point, Va.

Hamrick, J. M. (1992b), Estuarine environmental impact assessment using a three-dimensional circulation and transport model, in *Proceedings of the 2nd International Conference on Estuarine and Coastal Modeling*, edited by M. L. Spaulding et al., pp. 292-303, Am. Soc. of Civ. Eng., N. Y.

He, X., Y. Bai, D. Pan, N. Huang, X. Dong, J. Chen, C. T. A. Chen, and Q. Cui (2013), Using geostationary satellite ocean color data to map the diurnal dynamics of suspended particulate matter in coastal waters, *Remote Sens. Environ.*, *133*, 225–239.

Houwing, E. J., and L. C. Van Rijn (1998), In Situ Erosion Flume (ISEF): determination of bed shear stress and erosion of a kaolinite bed, *J. Sea Res.*, *39*, 243–253.

Houwing, E. (1999), Determination of the critical erosion threshold of cohesive sediments on intertidal mudflats along the Dutch Wadden Sea coast, *Estuarine Coastal Shelf Sci.*, *49*(4), 545–555.

Hu, K., P. Ding, Z. Wang, and S. Yang (2009), A 2D/3D hydrodynamic and sediment transport model for the Yangtze Estuary, China, *J. Mar. Syst.*, *77*(1-2), 114–136.

HydroQual Inc. (2002), *A Primer for ECOMSED User Manual*, Mahwah, N. J.

Jacobs, W., P. Le Hir, W. Van Kesteren, and P. Cann (2011), Erosion threshold of sand–mud mixtures, *Cont. Shelf Res.*, *31*(10), suppl., S14–S25, doi:10.1016/j.csr.2010.05.012.

Kandiah, A. (1974), Fundamental aspects of surface erosion of cohesive soils, PhD dissertation, Univ. of Calif., Davis.

Kim, S. C., C. T. Friedrichs, J. P.-Y. Maa, and L. D. Wright (2000), Estimating bottom stress in tidal boundary layer from acoustic Doppler velocimeter data, *J. Hydraul. Eng.*, *126*(6), 399–406.

Kong, Y. Z., P. Ding, S. He, C. He, and W. Xiao (2006), Analysis of Spatial and Temporal Variation Characteristics of Suspended Sediment Concentration in the Changjiang River Eatuary and Adjacent Sea Area [in Chinese with English abstract], *Adv. Mar. Sci.*, *24*(4), 446–454.

Lee, B. J., E. Toorman, F. Molz, and J. Wang (2011), A two-class population balance equation yielding bimodal flocculation of marine or estuarine sediments, *Water Res.*, *45*, 2131–2145.

Letter, J. V. J., and A. J. Mehta (2011), A heuristic examination of cohesive sediment bed exchange in turbulent flows, *Coastal Eng.*, *58*(8), 779–789, doi:10.1016/j.coastaleng.2011.04.003.

Li, J., and C. Zhang (1998), Sediment resuspension and implications for turbidity maximum in the Changjiang Estuary, *Mar. Geol.*, *148*(3), 117–124.

Liu, G., J. Zhu, Y. Wang, H. Wu, and J. Wu (2011), Tripod measured residual currents and sediment flux: Impacts on the silting of the Deepwater Navigation Channel in the Changjiang Estuary, *Estuarine Coastal Shelf Sci.*, *93*(3), 192–201, doi:10.1016/j.ecss.2010.08.008.

Lopes, J. F., J. M. Dias, and I. Dekeyser (2006), Numerical modelling of cohesive sediments transport in the Ria de Aveiro lagoon, Portugal, *J. Hydrol.*, *319*(1-4), 176–198, doi:10.1016/j.jhydrol.2005.07.019.

Luyten, P. J., J. E. Jones, R. Proctor, A. Tabor, P. Tett, and K. Wild-Allen (1999), COHERENS – A Coupled Hydrodynamical-Ecological Model for Regional and Shelf Seas: User Documentation. MUMM Report, Management Unit of the Mathematical Models of the North Sea, 914 pp.

Lumborg, U. (2005), Modelling the deposition, erosion, and flux of cohesive sediment through Øresund, *J. Mar. Syst.*, *56*(1-2), 179–193, doi: 10.1016/j.jmarsys.2004.11.003.

Maa, J., C. H. Lee, and F. J. Chen (1995), Bed shear stress measurements for VIMS Sea Carousel, *Mar. Geol.*, *129*(1–2), 129–136, doi:10.1016/0025-3227(95)00102-6.

Maa, J., J. Kwon, K. Hwang, and H. Ha (2008), Critical bed-shear stress for cohesive sediment deposition under steady flows, *J. Hydraul. Eng.*, *134*, 1767.

Madsen, O. S. (1994), Spectral wave–current bottom boundary layer flows, in *Proceedings of the 24th International Conference on Coastal Engineering Research Council*, Billy L. Edge, pp. 384–398, Kobe, Japan, Amer. Soc. Civil Eng., N. Y.

Otsubo, K., and K. Muraoka (1988), Critical shear stress of cohesive bottom sediments, *J. Hydraul. Eng.*, *114*(10), 1241–1256.

Panagiotopoulos, I., G. Voulgaris, and M. B. Collins (1997), The influence of clay on the threshold of movement of fine sandy beds, *Coastal Eng.*, *32*, 19–43.

Pang, C. G., Z. S. Yang, and J. Zhang (2001), Distribution of sediment and its impacts on flow structure at Huanghe (Yellow River) estuary in flood season [in Chinese with an English abstract], *J. Sediment. Res.*, *4*, 47–52.

Parchure, T. M., and A. J. Mehta (1985), Erosion of soft cohesive sediment deposits, *J. Hydraul. Eng.*, *111*(10), 1308–1326.

Partheniades, E. (1962), A study of erosion and deposition of cohesive soils in salt water, PhD dissertation, Univ. of Calif., Berkeley.

Pinto, L., A. B. Fortunato, Y. Zhang, A. Oliveira, and F. E. P. Sancho (2012), Development and validation of a three-dimensional morphodynamic modelling system for non-cohesive sediments, *Ocean Modell.*, *57-58*, 1–14, doi:10.1016/j.ocemod.2012.08.005.

Qi, J., C. Chen, R. Beardsley, W. Perrie, G. Cowles, and Z. Lai (2009), An unstructured-grid finite-volume surface wave model (FVCOM-SWAVE): Implementation, validations and applications, *Ocean Modell.*, *28*(1-3), 153–166.

Ramakrishnan, R., and A. S. Rajawat (2012), Simulation of suspended sediment transport initialized with satellite derived suspended sediment concentrations, *J. Earth Syst. Sci.*, *121*(5), 1201–1213.

Righetti, M., and C. Lucarelli (2007), May the shields theory be extended to cohesive and adhesive benthic sediments?, *J. Geophys. Res.*, *112*, C05039, doi:10.1029/2006JC003669.

Rouse, H. (1938), Experiments on the mechanics of sediment suspension, in *Proceedings of the Fifth International Congress for Applied Mechanics*, pp. 550–554, Cambridge, Mass.

Ryu, J. H., H. J. Han, S. Cho, Y.-J. Park, and Y.-H. Ahn (2012), Overview of geostationary ocean color imager (GOCI) and GOCI data processing system (GDPS), *Ocean Sci. J.*, *47*(3), 223–233, doi:10.1007/s12601-012-0024-4.

Salehi, M., and K. Strom (2012), Measurement of critical shear stress for mud mixtures in the San Jacinto estuary under different wave and current combinations, *Cont. Shelf Res.*, *47*, 78–92, doi:10.1016/j.csr.2012.07.004.

Sarmiento, O. A., and M. A. Falcon (2006), Critical bed shear stress for unisize sediment, *J. Hydraul. Eng.*, *132*(2), 172–179, doi:10.1061/(ASCE)0733-9429(2006)132:2(172).

Shen, F., W. Verhoef, Y. X. Zhou, M. S. Salama, and X. L. Liu (2010), Satellite estimates of wide-range suspended sediment concentrations in Changjiang (Yangtze) estuary using MERIS data, *Estuaries Coasts*, *33*(6), 1420–1429, doi:10.1007/s12237-010-9313-2.

Shen, F., Y. X. Zhou, J. F. Li, Q. He, and W. Verhoef (2013), Remotely sensed variability of the suspended sediment concentration and its response to decreased river discharge in the Yangtze estuary and adjacent coast, *Cont. Shelf Res.*, *69*, 52–61.

Shen, H., J. Li, H. Zhu, M. Han, and F. Zhou (1993), Transport of the suspended sediment in the Changjiang Estuary, *Int. J. Sediment Res.*, *7*(3), 45–63.

Shi, Z., H. J. Zhou, S. L. Eittreim, and J. C. Winterwerp (2003), Settling velocities of fine suspended particles in the Changjiang Estuary, China, *J. Asian Earth Sci.*, *22*(3), 245–251.

Skempton, A. W. (1953), The colloidal activity of clay, in *Proceedings of the Third International Conference on Soil Mechanics and Foundation Engineering*, vol. I, pp. 57–61, Zurich, Switzerland.

Smerdon, E. T., and R. P. Beasley (1959), The tractive force applied to stability of open channels in cohesive soils, *Res. Bull. 715*, Univ. of Mo., Columbia.

Song, D., and X. H. Wang (2013), Suspended sediment transport in the Deepwater Navigation Channel, Yangtze River Estuary, China, in the dry season 2009: 2. Numerical simulations, *J. Geophys. Res. Oceans*, *118*, 5568–5590, doi:10.1002/jgrc.20411.

Song, D., X. H. Wang, Z. Cao, and W. Guan (2013), Suspended sediment transport in the Deepwater Navigation Channel, Yangtze River Estuary, China, in the dry season 2009: 1. Observations over spring and neap tidal cycles, *J. Geophys. Res. Oceans*, *118*, 5555–5567, doi: 10.1002/jgrc.20410.

Soulsby, R. L., A. J. Manning, J. Spearman, and R. J. S. Whitehouse (2013), *Marine geology. Mar. Geol.*, *339*, 1–12, doi:10.1016/j.margeo.2013.04.006.

Styles, R., and S. M. Glenn (2002), Modeling bottom roughness in the presence of wave-generated ripples, *J. Geophys. Res.*, *107*(C8), 3110, doi:10.1029/2001JC000864.

Thoman, R. W., and S. L. Niezgoda (2008), Determining erodibility, critical shear stress, and allowable discharge estimates for cohesive channels: Case study in the Powder River basin of Wyoming, *J. Hydraul. Eng.*, *134*(12), 1677–1687.

Torfs, H. (1995), Erosion of mud/sand mixtures, PhD dissertation, Katholieke Univ. Leuven, Leuven, Netherlands.

Van der Wal, D., T. Van Kessel, M. A. Eleveld, and J. Vanlede (2010), Spatial heterogeneity in estuarine mud dynamics, *Ocean Dyn.*, *60*(3), 519–533, doi:10.1007/s10236-010-0271-9.

Van Kessel, T., H. Winterwerp, B. Van Prooijen, M. Van Ledden, and W. Borst (2011), Modelling the seasonal dynamics of SPM with a simple algorithm for the buffering of fines in a sandy seabed, *Cont. Shelf Res.*, *31*, suppl., S124–S134, doi:10.1016/j.csr.2010.04.008.

Van Leussen, W. (1994), Estuarine macroflocs and their role in fine-grained sediment transport, PhD thesis, 488 pp., Univ. of Utrecht, Netherlands, Utrecht.

Van Prooijen, B. C., and J. C. Winterwerp (2010), A stochastic formulation for erosion of cohesive sediments, *J. Geophys. Res.*, *115*, C01005, doi:10.1029/2008JC005189.

Verney, R., R. Lafite, J. C. Brun-Cottan, and P. Le Hir (2011), Behaviour of a floc population during a tidal cycle: Laboratory experiments and numerical modelling, *Cont. Shelf Res.*, *31*, suppl. 10, S64–S83.

Wang, X. H. (2002), Tide-induced sediment resuspension and the bottom boundary layer in an idealized estuary with a muddy bed, *J. Phys. Oceanogr.*, *32*(11), 3113–3131.

Wang, X. H., and H. Wang (2010), Tidal straining effect on the suspended sediment transport in the Huanghe (Yellow River) Estuary, China, *Ocean Dyn.*, *60*(5), 1273–1283, doi:10.1007/s10236-010-0298-y.

Warner, J., C. Sherwood, R. Signell, C. Harris, and H. Arango (2008), Development of a three-dimensional, regional, coupled wave, current, and sediment-transport model, *Comput. Geosci.*, *34*(10), 1284–1306.

Whitehouse, R. J. S., R. L. Soulsby, W. Roberts, and H. J. Mitchener (2000), *Dynamics of Estuarine Muds*, Thomas Telford, London, U. K.

Wilcock, P. R. (1993), Critical shear stress of natural sediments, *J. Hydraul. Eng.*, *119*(4), 491–505.

Winterwerp, H. (1999), On the dynamics of high-concentrated mud suspensions, *Commun. Hydraul. Geotech. Eng. Rep. 99-3*, Delft Univ. of Technol., Netherlands, Delft.

Winterwerp, J. C., and W. G. Van Kesteren (2004), *Introduction to the Physics of Cohesive Sediment Dynamics in the Marine Environment*, Elsevier, Amsterdam, Netherlands.

Winterwerp, J. C., A. J. Manning, C. Martens, T. de Mulder, and J. Vanlede (2006), A heuristic formula for turbulence-induced flocculation of cohesive sediment, *Estuarine Coastal Shelf Sci.*, *68*, 195–207.

Winterwerp, J. C., W. G. M. van Kesteren, B. van Prooijen, and W. Jacobs (2012), A conceptual framework for shear flow–induced erosion of soft cohesive sediment beds, *J. Geophys. Res.*, *117*, C10020, doi:10.1029/2012JC008072.

Wu, L., C. Chen, P. Guo, M. Shi, J. Qi, and J. Ge (2011), A FVCOM-based unstructured grid wave, current, sediment transport model, I. Model description and validation, *J. Ocean Univ. China*, *10*(1), 1–8, doi:10.1007/s11802-011-1788-3.

Xue, P., C. Chen, P. Ding, R. C. Beardsley, H. Lin, J. Ge, and Y. Kong (2009), Saltwater intrusion into the Changjiang River: A model-guided mechanism study, *J. Geophys. Res.*, *114*, C02006, doi:10.1029/2008JC004831.

Yang, S. L., J. Zhang, S. B. Dai, M. Li, and X. J. Xu (2007), Effect of deposition and erosion within the main river channel and large lakes on sediment delivery to the estuary of the Yangtze River, *J. Geophys. Res.*,*112*, F02005, doi:10.1029/2006JF000484.

Zheng, L., C. Chen, M. Alber, and H. Liu (2003), A 3-D modeling study of the Satilla River estuarine System. Part II: Suspended sedimentation, *Estuaries*, *26*(3), 670–679.